www.sciencemag.org/content/364/6436/eaau8650/suppl/DC1

Supplementary Materials for

The NASA Twins Study: A multidimensional analysis of a year-long human spaceflight

Francine E. Garrett-Bakelman, Manjula Darshi, Stefan J. Green, Ruben C. Gur, Ling Lin, Brandon R. Macias, Miles J. McKenna, Cem Meydan, Tejaswini Mishra, Jad Nasrini, Brian D. Piening, Lindsay F. Rizzardi, Kumar Sharma, Jamila H. Siamwala, Lynn Taylor, Martha Hotz Vitaterna, Maryam Afkarian, Ebrahim Afshinnekoo, Sara Ahadi, Aditya Ambati, Maneesh Arya, Daniela Bezdan, Colin M. Callahan, Songjie Chen, Augustine M. K. Choi, George E. Chlipala, Kévin Contrepois, Marisa Covington, Brian E. Crucian, Immaculata De Vivo, David F. Dinges, Douglas J. Ebert, Jason I. Feinberg, Jorge A. Gandara, Kerry A. George, John Goutsias, George S. Grills, Alan R. Hargens, Martina Heer, Ryan P. Hillary, Andrew N. Hoofnagle, Vivian Y. H. Hook, Garrett Jenkinson, Peng Jiang, Ali Keshavarzian, Steven S. Laurie, Brittany Lee-McMullen, Sarah B. Lumpkins, Matthew MacKay, Mark G. Maienschein-Cline, Ari M. Melnick, Tyler M. Moore, Kiichi Nakahira, Hemal H. Patel, Robert Pietrzyk, Varsha Rao, Rintaro Saito, Denis N. Salins, Jan M. Schilling, Dorothy D. Sears, Caroline K. Sheridan, Michael B. Stenger, Rakel Tryggvadottir, Alexander E. Urban, Tomas Vaisar, Benjamin Van Espen, Jing Zhang, Michael G. Ziegler, Sara R. Zwart, John B. Charles*, Craig E. Kundrot*, Graham B. I. Scott*, Susan M. Bailey*, Mathias Basner*, Andrew P. Feinberg*, Stuart M. C. Lee*, Christopher E. Mason*, Emmanuel Mignot*, Brinda K. Rana*, Scott M. Smith*, Michael P. Snyder*, Fred W. Turek*

*Corresponding author. Email: jbcharle@gmail.com (J.B.C); craig.e.kundrot@nasa.gov (C.E.K.); graham_b_scott@yahoo.com (G.B.I.S.); susan.bailey@colostate.edu (S.M.B.); basner@pennmedicine.upenn.edu (M.B.); afeinberg@jhu.edu (A.P.F.); stuart.lee-1@nasa.gov (S.M.C.L.); chm2042@med.cornell.edu (C.E.M.); mignot@stanford.edu (E.M.); bkrana@ucsd.edu (B.K.R.); scott.m.smith@nasa.gov (S.M.S.); mpsnyder@stanford.edu (M.P.S.); fturek@northwestern.edu (F.W.T.)

Published 12 April 2019, *Science* **364**, eaau8650 (2019)
DOI: 10.1126/science.aau8650

This PDF file includes:

Other Supporting Online Material for this manuscript includes the following:
(available at www.sciencemag.org/content/364/6436/eaau8650/suppl/DC1)

Tables S1 to S6, S8, and S9 (Excel)

Materials and Methods

Study Subjects' consent

Study subjects signed informed consent according to the declaration of Helsinki and 14 CFR Part 1230 for collection and use of sample materials and data in research protocols at NASA and the collaborating institutions. Study protocols were approved by the NASA Flight Institutional Review Board (protocol number Pro1245) and all participating institutions.

Blood sample collection for plasma, DNA and RNA extraction

Sample collection. Blood samples were collected from flight (TW) and ground (HR) subjects into 4 mL CPT vacutainers (BD Biosciences Cat # 362760) per manufacturer's recommendations. Cell separation was performed by centrifugation at 1800 X g for 20 min at room temperature, both for the ISS and ground-based samples. Ambient blood collected samples slated for immediate return on the Soyuz capsule were stored at 4°C until processing (average of 35-37 hours after collection, including repatriation time). Samples collected on Earth and on the ISS and planned for long-term storage were mixed by inversion and immediately frozen at -80◦C.

Fresh processing of CPT tubes was performed using the following steps: 1) plasma was retrieved from the CPT tubes and flash frozen prior to long term storage at -80°C. 2) Cells were subjected to positive selection for CD4 cells using magnetic beads (Miltenyi Biotec Cat # 130-097-048) per manufacturer's recommendations. 3) Flow through from the CD4 cell selection was subjected to positive selection for CD8 cells using magnetic beads (Miltenyi Biotec Cat # 130-097-057) per manufacturer's recommendations. And 4) Flow through from the CD8 selection was subjected to CD19 cell positive selection using magnetic beads (Miltenyi Biotec Cat # 130-097-055) per manufacturer's recommendations. The flow through from the last step (Lymphocytes depleted fraction; LD) was recovered. Validation of cell separation approach was performed on a blood sample from a healthy volunteer (**Fig. S1**). CD4, CD8, CD19 and LD cells were divided into cell pellets and RLT+ buffer (Qiagen Cat # 80204) lysates, flash frozen and stored at -80°C until use. Frozen CPTs were thawed at 37°C; 1:10 volume of 1mg/mL DNase (Sigma) was added to each supernatant and incubated at 37°C for 90 seconds. Supernatant was recovered. Cells were pelleted by centrifugation at 300 X g, washed in 4°C PBS and lysed into RLT+ buffer, flash frozen and stored at -80°C until use.

Nucleic acid extractions and quality control. QIAGEN's Allprep kit (Cat # 80204) was used for DNA and RNA extraction from RLT+ lysates per manufacturer's recommendations. DNA was extracted from cell pellets using Epicentre masterpure kit per manufacturer's recommendations (Lucigen Cat # MCD85201). Quantitation of RNA and DNA was assessed using Qubit 2.0 (Invitrogen) per manufacturer's recommendations. DNA quality was assessed by visualization on 0.7% agarose gels using standard techniques. RNA quality control was performed using RNA Nano kit (Agilent) on a Bioanalyzer 2100 (Agilent) per manufacturer's recommendations. Quality control of RNA extracted from CPT tubes and collection details are in **Table S9** All samples were processed at Johnson Space Center unless otherwise noted. Plasma from the CPT tubes was used for proteomics studies; DNA and RNA from these extractions was used for gene expression, TCR sequencing, DNA methylation assays and telomere length assessments. RNA quality results (RIN scores) are included in **Table S9**.

Ambient return controls. To control for ambient return effects on molecular signatures, we generated control samples that represented the fresh (FR) and ambient return (AR) sample collection conditions.

Blood was collected from a male volunteer of similar age and ethnicity to the study subjects, in three 4 mL CPT vacutainers (BD Biosciences Cat # 362760) per manufacturer's recommendations and centrifuged at 1800 X g for 20 minutes at room temperature. One vacutainer was used as a FR control, and processed as per the protocol for freshly processed CPT tubes. The remaining two vacutainers were used for AR controls. To simulate temperature and storage conditions during ambient return, AR controls were shipped at 4°C via Fedex for 3000 flight miles, re-packed and shipped again for 3000 flight miles, before being processed in the same manner as the FR control. The duration between collection and processing of AR samples was 48 hours. Data generated from AR and FR controls were used to normalize the gene expression data for any confounding effects of ambient return using ComBat or multivariate models in differential expression analysis (*85*). Correction process is explained in methods for transcriptome analysis.

Telomere length, Telomerase activity and Chromosome assays

Processing for qPCR-based assessment of Telomere Length and Telomerase Activity. Blood samples were collected into K_2EDTA tubes on Earth or on the ISS and processed per manufacturer's recommendations (BD Biosciences Co #368589), stored at room temperature and shipped to Colorado State University. On arrival cells were transferred into CPT mononuclear cell preparation tubes (Becton, Dickinson, and Co # 362761) and centrifuged at 1700 x g for 20 min per manufacturer's recommendations. Separated peripheral blood mononuclear cells (PBMCs) were collected and washed in PBS and any remaining red blood cell contamination was removed using ACK lysis buffer (*86*). PBMCs ($1x10^6$ cells / mL) were divided for either qRT-PCR based-telomere length measurement or qRT-PCR TRAP. DNA extraction for qPCR telomere length measurements was performed using the DNeasy Blood and Tissue Kit (Qiagen #69504). PBMCs were initially incubated in proteinase K for 3 h at 37°C. DNA isolated from CD4+ and CD8+ T-cells, CD19+ B-cells, lymphocyte depleted (LD), and whole PBMC populations was also used. For telomerase activity, PBMC protein lysates were prepared in mammalian protein extraction buffer (M-PER) (ThermoFisher #78503) containing cOmplete Protease Inhibitor Cocktail (Millipore Sigma #11836170001) and RNasin Ribonuclease Inhibitors (Promega #N2515) at $1x10^6$ cells per 100 µL. Lysates were cleared by incubating on ice for 10 min, followed by centrifugation at 18,000 rpm for 15 min at 4°C, aliquoted, and stored at -80°C. Protein concentration was determined using the Bio-Rad Protein Assay Kit (Bradford Assay; Bio-Rad # 5000001).

Sample Collection and Blood Stimulation for Telo-FISH and dGH. Peripheral blood was drawn and collected in one 10 mL sodium heparin tube (Becton, Dickinson, and Co #367874) and one 10 mL ethylenediaminetetraacetic acid (K_2EDTA) tube (Becton, Dickinson, and Co #368589). Samples were shipped under ambient conditions and received at Colorado State University (CSU) within 24 h of blood draw. Heparinized blood was split into two T-25 tissue culture flasks, 1:9 in Gibco PB-Max Karyotyping Medium supplemented with phytohaemagglutinin A (PHA) (ThermoFisher #12557021). For Directional Genomic Hybridization (dGH), 5.0 mM 5-bromo-deoxyuridine (BrdU) and 1.0 mM 5-bromo-deoxycytidine (BrdC) were added to the medium (*29*). Following 44 hr incubation/stimulation, KaryoMax Colcemid (ThermoFisher #15210040) was added [0.1 µg/mL final concentration] for the final four hours prior to harvest (at 48 h), then metaphase chromosome spreads were prepared using standard cytogenetic techniques (e.g. (*87*)).

Multiplexed Quantitative PCR Telomere Length Measurement. Multiplexed qPCR measurements of telomere length were carried out as previously described (*20*). Here, a 22 µL master mix was prepared using SYBR green GoTaq qPCR master mix (Promega #A6001) combined with the telomere forward primer (TelG; 5'-ACACTAAGGTTTGGGTTTGGGTTTGGGTTTGGGTTAGTGT-3'), telomere reverse primer (TelC; 5'-TGTTAGGTATCCCTATCCCTATCCCTATCCCTATCCCT AACA-3'), albumin forward primer (AlbU; 5'-CGGCGGCGGGCGGCGCGGGCTGGGCGGA AATGCTGCACAGAATCCTTG-3'), albumin reverse primer (AlbD; 5'-GCCCGGCCCGCCG

CGCCCGTCCCGCCGGAAAAGCATGGTCGCCTGTT-3') at 10 μM per primer (Integrated DNA Technologies), and RNase/DNase free water. To the master mix, 3 μL of DNA at 3.33 ng/uL was added for a final volume of 25 μL. The TelG/C primers were at a final concentration of 900 nM and the AlbU/D primers at 400 nM.

Telomere length measurements were carried out using a Bio-Rad CFX-96 qPCR machine. The cycle design was as follows: 95°C for 3 min; 94°C for 15 s, 49°C for 15 s, for 2 cycles; 94°C for 15 s, 62°C for 10 s, 74°C for 15 s, 84°C for 10 s, and 88°C for 15 s, for 32 cycles. The melting curve was established by a 72°C to 95°C ramp at 0.5°C/second increase with a 30 second hold. Multiplexing both telomere and albumin primers using a single fluorescent DNA-intercalating dye is possible because the telomere sequences are amplified at a lower quantification cycle (Cq) than the albumin sequences. Standard curves were prepared using human genomic DNA (Promega Cat # G3041) with 3-fold dilutions ranging from 50 ng to 0.617 ng in 3 μL per dilution. Negative controls included a no-template TelG/C only and AlbU/D only, and a combined TelG/C and AlbU/D control. Samples were normalized across plates using a human genomic DNA standard. Each sample was run in triplicate on a 96-well plate format and relative telomere length was established using a telomere (T) to albumin (A) ratio.

Quantitative Real Time PCR (qRT-PCR) Telomere Repeat Amplification Protocol (TRAP). Telomerase activity was monitored using qRT-PCR TRAP as previously described (*26*). Here, protein lysates were suspended at 0.20 μg in 25 μL of SYBR green GoTaq qPCR master mix (Promega #A6001) containing 0.20 μg T4 gene 32 protein (New England Biolabs #M0300S), 0.10 μg of primers TS (5'-AATCCGTCGAGCAG AGTT- 3') and ACX (5'-GCGCGG(CTTACC)$_3$CTAACC-3') (Integrated DNA Technologies) and RNase/DNase free water. The qRT PCR reactions took place using a Bio-Rad CFX-96 qPCR machine using the following steps: 25ºC for 20 min; 95ºC for 3 min; 95ºC for 20 s, 50ºC for 30 s, 72ºC for 90 s for 50 cycles; establish a melting curve and prevent primer dimerization for 10 s per cycle for 80 cycles. Each sample was run in triplicate on a 96-well plate format allowing for an average Cq to be obtained per sample. Relative telomerase activity was then established using the delta delta Ct method (*88*). In addition to the test samples, the following controls were included: no template controls with TS only, ACX only, and TS/ACX primers combined, as well as a HeLa cell line (ATTC CCL-2) heat-inactivated negative control, and a HeLa positive control (very high telomerase activity).

Telomere Fluorescence in situ Hybridization (Telo-FISH). Prepared slides with metaphase chromosome spreads were hybridized with a fluorescently-labeled telomere probe as previously described (*24*). Briefly, slides were washed in PBS for 5 min, dehydrated through a cold ethanol series (75%, 85% and 100%) for 2 min each, and air dried. Slides were then denatured in 70% formamide/2x sodium chloride and sodium citrate (2xSSC) at 75°C for 2 min, followed by a second cold ethanol series. A hybridization mixture containing a G-rich (TTAGGG$_3$) peptide nucleic acid (PNA) telomere probe directly labeled with Cyanine-3 (Cy3; Biosynthesis) was prepared by diluting 0.5 μL probe [5nM final concentration] in 36 μL of formamide, 12 μL of 0.5 M pH 7.5 Tris-HCl, 2.5 μL of 0.1 M KCl, and 0.6 μl of 0.1 M $MgCl_2$; mixture was incubated at 75°C for 5 min, then 50 μL applied to each slide. Coverslips were sealed with rubber cement and slides incubated at 37 °C for 18 h. After hybridization, slides were washed in a series of 43.5°C washes for three min each: washes one and two: 50% formamide in 2x sodium chloride and sodium citrate (2xSSC); washes three and four: 2x SSC; and washes five and six: 2x SSC plus 0.1% Nonidet P-40. Slides were counterstained with 50 μL DAPI in Prolong Gold Antifade (ThermoFisher #P36931), coverslipped, and stored at 4°C.

Metaphase spreads (30-50 per sample) were imaged on a Nikon Eclipse Ni-U epifluorescent microscope equipped with an Andor Zyla 5.5 sCMOS camera and SpectraX LED light source. Stacked images (5 images/stack, 0.3 μm step size) were taken of each metaphase spread. Fluorescence intensity was then quantified using the ImageJ (http://rsb.info.nih.gov/ij/) plugin, Telometer

(http://demarzolab.pathology.jhmi.edu/telometer/index.html), and normalized using the mouse lymphoma control cell line, LY-S [as per (*89*)].

Directional Genomic Hybridization (dGH). High resolution detection of inversions and translocations was performed utilizing Directional Genomic Hybridization (dGH) single color (Cy-3) whole chromosome 1-3 paints (KromaTiD Inc., Ft. Collins, CO) as previously described (*29, 30*). Briefly, prepared slides with metaphase chromosomes substituted with bromonucleotides (BrdU/BrdC) were submersed in Hoechst 33258 (Millipore Sigma #B1155) for 15 min, selectively photolysed using a SpectroLinker UV Crosslinker equipped with 365 nm UV bulbs for 35 min, and then the nicked DNA was exonucleolytically degraded with Exonuclease III (New England Biolabs #M0206L) for 30 min. Hybridization cocktail was applied to the slides, which were coverslipped and sealed using rubber cement, then denatured at 68°C for three min. Slides were hybridized overnight at 37°C followed by five washes in 2x SSC at 43°C prior to imaging. Metaphase spreads were imaged on a Nikon Eclipse Ni-U epifluorescent microscope equipped with an Andor Zyla 5.5 sCMOS camera and SpectraX LED light source. Stacked images (5 images/stack, 0.3 μm step size) were taken of ~ 50 metaphase spreads per sample. Statistical significance was established using a two-tailed Student's t-test or one-way ANOVA for multiple comparisons on GraphPad Prism 5 software for Windows. Normality was assessed prior to running the t-tests. A Wilcoxon rank sum test was used to test for significant differences in medians between telomere length RFI distributions.

Whole genome bisulfite sequencing (WGBS)

Library preparation. WGBS single indexed libraries were generated using NEBNext Ultra DNA library Prep kit for Illumina (New England BioLabs, Ipswich, MA, USA) according to the manufacturer's instructions with modifications. Genomic DNA (300 ng) was quantified with the Qubit dsDNA BR assay (Invitrogen, Carlsbad, CA, USA) and fragmented using a Covaris S2 sonicator to an average insert size of 350 bp. Size selection was performed using AMPure XP beads and insert sizes of 300-400 bp were isolated. Samples were bisulfite converted after size selection using EZ DNA Methylation-Gold Kit (Cat# D5005, Zymo, Irvine, CA, USA) following the manufacturer's instructions. Amplification was performed after the bisulfite conversion using Kapa Hifi Uracil+ (Cat# KK282, Kapa Biosystems, Boston, USA) polymerase using the following cycling conditions: 98°C 45s; 10 cycles of 98°C 15s, 65°C 30s, 72°C 30s; and 72°C one min.

Final libraries were analyzed on a 2100 Bioanalyzer (Agilent, Santa Clara, CA, USA) using the High-Sensitivity DNA assay for quality control purposes. Libraries were quantified by qPCR using the Library Quantification Kit for Illumina sequencing platforms (Cat# KK4824, KAPA Biosystems, Boston, USA), using a 7900HT Real Time PCR System (Applied Biosystems). Each library was sequenced in one lane with Illumina HiSeq2500 sequencer using 125 bp paired-end reads and 10% PhiX spike-in. Sequencing statistics are included in **Table S11**.

Mapping and quality control of WGBS reads. Trim Galore! (v0.4.0; http://www.bioinformatics.babraham.ac.uk/projects/trim_galore/) was used to quality-trim reads and trim adapter sequences using the following parameters: trim_galore -q 25 --paired ${READ1} ${READ2}. These trimmed reads were then aligned to the hg19 build of the human genome (including autosomes, sex chromosomes, mitochondrial sequence, and lambda phage (accession NC_001416.1) but excluding non-chromosomal sequences) by employing Bismark (*90*) (v0.14.3) with the following alignment parameters: bismark --bowtie2 -X 1000 -1 ${READ1} -2 ${READ2}. Using the reads aligned to the lambda phage genome, all libraries were estimated to have a bisulfite conversion rate > 99%.

The bismark_methylation_extractor tool of Bismark (*90*) was used to summarize the number of reads supporting a methylated cytosine and the number of reads supporting an unmethylated cytosine for every cytosine in the reference genome. To do so, the M-bias (*91*) of the libraries were first computed and visually inspected and resulted in ignoring the first 2 bp of read1 and the first 4-12 bp of read2 depending on the sample (e.g. bismark_methylation_extractor --ignore 2 --ignore_r2 4). The final cytosine report file summarizes the methylation evidence at each cytosine in the reference genome.

BSmooth was applied to the Bismark results to estimate CpG methylation levels as previously described (*91*). Smoothing over windows of at least 1 kb containing at least 20 CpGs was applied and all CpGs that had a sequencing coverage of at least 5 in all 8 samples were analyzed. These data were then used to perform principal component analysis (PCA). In addition, informME (v0.2.2), an information theoretic approach to methylation modeling and analysis (*33, 92*) was applied to compute mean methylation levels (MMLs) as measures of average methylation, normalized methylation entropies (NMEs) as measures of methylation stochasticity, and Jensen-Shannon distances (JSDs) as measures of epigenetic dissimilarities between samples.

The gene ranking function, rankGenesEmpNull, of informME v0.2.2, was employed to rank all genes in the genome that are subject to epigenetic discordance in methylation for all relevant comparisons. This function performs ranking by using the JSD values within a fixed window (here 2 kb upstream and 5 kb downstream of the transcription start site, TSS) and hypothesis testing. The required null distribution was computed empirically by comparing the two subjects preflight. To combine multiple ranked lists into a single ranking, the rank product method was used (*93*). Moreover, gene ontology (GO) enrichment analysis was performed using GOrilla's single ranked lists method with the "fast mode" option disabled (*94, 95*). GO categories with fewer than five genes in the GO database or with a q-value greater than 0.05 were removed.

Transcriptome Preparation, Sequencing, and Analysis

RNA-seq library preparation and sequencing for Ribodepleted RNA. RNA Ribo-depletion preparations were performed with the NEBNext® Ultra™ II Directional RNA Library Prep Kit for Illumina® (E7760/E7765) and NEBNext rRNA Depletion Kit (NEB #E6310) as well as hemoglobin depletion reagents (courtesy of New England Biolabs) according to product manuals. Input RNA was high-quality (RIN ~8-9) so the full fragmentation time (15 minutes) was applied. 25 ng of input RNA was used for all samples; adapters were diluted 25-fold during library preparation steps. Universal Human reference RNA (UHRR) with ERCC spike-in was used as control RNA to ensure library quality. No size selection step was applied during any bead cleanups for these samples. 13 cycles of PCR were optimal for this input, generating sufficient library for sequencing without overproduction of PCR duplicates. Sample indexing was carried out with the NEBNext® Multiplex Oligos for Illumina® (96 Index Primers) barcode plate (E6609S) as well as additional standard barcodes (#10-15, 18-23, 27-28 from Multiplex Oligos for Illumina® Index Primers Sets 1,2,3 [E7335S,E7500S,E7710S]), and all samples were sequenced as one pool across two full flow cells, PE 150x150 on the Illumina HiSeq4000.

RNA-seq library preparation and sequencing for PolyA RNA. PolyA RNA preparations were performed with the NEBNext® Ultra™ II Directional RNA Library Prep Kit for Illumina® (E7760/E7765) and NEBNext Poly(A) mRNA Magnetic Isolation Module (NEB #E7490). Input RNA was high-quality (RIN ~8-9; Table S9, however, longer fragments were desired for this approach so a shorter fragmentation time (8 min) was applied. 50 ng of input RNA was used; adapters were accordingly diluted 25-fold during library preparation steps. UHRR with ERCC spike-in was again used as control RNA to ensure library quality. In accordance with the desired longer library inserts, a size selection step was applied during the

bead cleanup just prior to PCR for these samples: 20 uL of magnetic SPRIselect beads were added to the ligation reaction to remove the largest fragments only. The supernatant was transferred to clean tubes and 10 uL of fresh beads were added. Magnetic separation, subsequent supernatant aspiration, and wash steps were carried out normally. Sixteen cycles of PCR were used to generate sufficient library for sequencing. Sample indexing was carried out with the NEBNext® Multiplex Oligos for Illumina® (96 Index Primers) barcode plate (E6609S) as well as additional standard barcodes (#10-15, 18-25, 27-29) from Multiplex Oligos for Illumina® Index Primers Sets 1,2,3 [E7335S,E7500S,E7710S]) and all samples were sequenced as one pool across two full flow cells, PE 150x150 on the Illumina HiSeq4000. RNA-sequencing statistics are included in **Table S9.**

Purified and bulk-cell populations from both twins were processed for for RNA-sequencing libraries (polyA and ribo-seq) using standard NEB protocols and matching input amounts for all samples, including with randomized barcodes, library preparation protocols, and a uniform pool of samples for sequencing to minimize any batch effects. QC was performed using FastQC and MultiQC on the raw and processed files (*96, 97*). Adapter removal was performed using Trim Galore! (v0.4.1) (*98, 99*). Reads were aligned to hg19 genome and Gencode v19 gene reference (including ERCC spike-in contigs, Thermofisher Cat.# 4456740) with STAR transcriptome aligner (v2.5.1b) using two-pass alignment (where the second-pass reference to fine tune junction points was created by pooling junctions of all samples together) (*100, 101*). Aligned reads were quantified using subread featureCounts and kallisto on ENSEMBL transcripts and summarizing results from each transcript into their respective genes (*102-104*). Same process was followed for UHRR control samples and ambient control samples.

Differential gene expression analysis was performed using DESeq2 on uncorrected and unnormalized gene counts (*105*). Main analysis for **Fig. 1B** was performed using all samples together to control for subject, Inflight and Postflight specific changes and effects of ambient return. In this comparison, all samples of HR were taken as to control the normal variance within gene expression levels during the year-long period. Preflight samples from TW were used to set the baseline expression for TW. Inflight and postflight samples of TW were compared to these baselines in a multivariate model, also accounting for ambient return effects as mentioned below. Each cell type was treated separately. Two different library preparations for PolyA+ and rRNA depletion were combined together with an added covariate in the multivariate model. Other, more specific comparisons were also performed, for example comparing Inflight period to pre- and postflight periods in TW. Details for these comparisons and results are provided in **Table S2**. The number of genes that stayed perturbed after landing were calculated as any gene that was not differentially expressed in "Inflight vs Postflight" comparison but was significantly differentially expressed in at least two out of three comparisons that include "Inflight vs Preflight", "Postflight vs Preflight" and "Inflight+Postflight vs Preflight", all matching in the directionality of gene expression change ($q < 0.05$). This list was further filtered by removing any gene that was differentially expressed between TW preflight and all HR samples. This was done to remove any gene that might be altered during TW preflight prior to launch, but returned to baseline levels comparable to HR during inflight and postflight. This resulted in 744 genes across CD4, CD8, and LD cells that were altered during flight and stayed perturbed postflight. PBMCs were excluded from this analysis due to missing preflight samples.

Differential gene expression results were sorted by the wald statistic from DESeq2 output and Gene Set Enrichment Analysis (GSEA) was performed using fgsea on Molecular Signatures Database and MGI Mouse Phenotypes (*106-109*). Results were filtered for $q < 0.01$ and reported in **Table S2**.

All inflight samples for TW in CD4, CD8, CD19 and LD cells were ambient returns. R+0 sample immediately after landing was used to model the effects of ambient return without fully confounding the term with inflight duration. GD 298 sample for HR was also subjected to shipping prior to processing at an ambient temperature.

In differential expression analysis multivariate models, a term was added that included ambient and fresh samples for TW, HR as well as the simulated ambient control for a given cell type and library preparation to correct any systematic changes to gene expression that might arise due to ambient return. In comparisons where not all subjects would be included (such as late-flight vs early-flight just for TW), a minimal set of ambient return correction samples were included (HR: GD 298 (AR-like), GD+2 FR, GD+65 FR; TW: FD 340 (AR), R+0; in addition to the fresh and simulated ambient samples from the control subject).

For other analyses and visualization gene counts were normalized using TMM (*110*). In CD4, CD8, CD19 and LD cells where expression results were confounded by ambient return, ComBat was used to correct for the potential batch effect. Correction was carried out using AR, FR samples from HR and TW, as well as the additional control subject (*111, 112*). To ensure unbiased results the correction was applied by subject identity (TW, HR or control subject) and was blinded to flight status and other covariates of interest (*113*). Unsupervised embedding of samples was performed using t-statistic distributed stochastic neighbor embedding (t-SNE) on TMM normalized and ambient return corrected expression values, shown in **Fig. S2** (*114*).

Quantification of mtRNA by RT-qPCR: 100ng RNA per sample was reverse transcribed using the iScript Advanced cDNA synthesis kit (Bio-Rad) as per manufacturer's instructions. The synthesized cDNA was diluted 1:4 in water and quantitative PCR was performed in triplicate with the Power SYBR Green PCR master mix (Thermo-Fisher) using the QuantStudio 6 Flex RT-PCR system. The sequences of primers used for RT-qPCR were: *MT-CO1* forward primer (5'-CAGCAGTCCTACTTCTCCTATCTCT-3') and reverse primer (5'-GGGTCGAAGAAGGTGGTGTT-3'), *18S* forward primer (5'-GGCCCTGTAATTGGAATGAGTC-3') and reverse primer (5'-CCAAGATCCAACTACGAGCTT-3'), and *GAPDH* forward primer (5'-AAGGTGAAGGTCGGAGTCAAC-3') and reverse primer (5'-GGGGTCATTGATGGCAACAATA-3').

T-Cell Receptor (TCR) sequencing

Samples were obtained from the pair of identical twins before and ~10 days after a trivalent Influenza Vaccine (3 strains, 2015 Fluzone intradermal from SANOFI PASTEUR INC.; see **Table S1** for dates of collection) flu immunization over a three-year period. One of the twins was sampled on Earth years 1 and 3, the year 2 sample was collected in the International Space Station (ISS) while the other twin was sampled on Earth all 3 years. For samples collected on earth, CD4+ and CD8+ T cells were separated and repertoires for these cell populations analyzed independently. Because the samples from space were frozen, we also froze samples collected on Earth for comparison. The frozen sample was expected to give a mix of CD4+ and CD8+ repertoires.

Total RNA of CD4+ and CD8+ cells from fresh blood and RNA from CPT frozen blood were used to amplify TCR-α/β repertoires covering both the V and J segments (*115*). The libraries of amplified α and β repertoire were sequenced by Illumina high throughput sequencing system 2x150 HiSeq4000. Briefly, the quality of raw FASTQ files were assessed using FASTQC (*97*). Post quality control, FLASH was used to merge the paired end reads (*116*). Blast databases were constructed from IMGT TCR α/β sequences using local blast binaries (*117*). The resulting fasta file was used to query the BLAST database and identify the TCR C, J & V Regions. The CDR3s were extracted and their frequency along with usage of V, J families was computed. Vaccination responsive clones were identified by matching CDR3s pre-and post-vaccination for each subject and cell type, with z scores as measures of change using a one tailed approach.

A 5% False Discovery Rate threshold was calculated and clones that met this threshold considered vaccination-responsive clones. CD4+ and CD8+ cells profiled in both subjects year 1 and year 3 (i.e. ground time points) bracketing year 2 (when the space mission occurred) were used in each subject to determine clones that were consistently responsive to vaccination within CD4+ and CD8+ cell subsets. These series of responsive clones were next used to quantify vaccine responses in each subject during season 2, in flight for twin 1 and on ground twin 2 using CPT tubes (fresh cells could not be isolated in the ISS). Because Year 2 in-flight post-vaccination frozen CPT samples had poor TCR diversity and yield due to harsh conditions in the space station, TCR clones were down-sampled for the on-ground year 2 frozen CPT to the number of clones that were vaccination responsive in year 2 in-flight subject. In TW (the flight subject) for inflight vaccination timepoints, we identified 291 (3.7%) and 192 (1.6%) clones as increased from TCR alpha and beta respectively in the CPT tube. We used these numbers to downsample the ground-based twin's CPT season 2 vaccination clones, while we initially identified 547 (1.4%) and 2,516 (4.3%) clones as increased from TCR alpha and beta respectively in the CPT tube in the season 2 ground-based vaccination, we downsampled these to the top 291 and 192 clones from alpha and beta respectively. This ensured fair comparison. The proportion of vaccination responsive CPT clones (year 2) in both flight and ground subject (present in each respective CD4+/CD8+ vaccination responsive database of each subject, see above) were finally compared between the flight and ground subjects.

Proteomics

Targeted Urine Proteomics. An LC-MS/MS based targeted proteomic approach was applied to assess 24 hour pooled urine samples targeting a panel of 20 proteins which are found detectable in urine samples derived from healthy subjects and individuals with pathological conditions: podocalyxin (PODXL), renin receptor (RENR), urokinase-type plasminogen activator (UROK), pro-epidermal growth factor (EGF), Collagen alpha-1(I) chain (CO1A1), Collagen alpha-1(III) chain (CO3A1), Intercellular adhesion molecule 1 (ICAM1), Cathepsin D (CATD), Matrilysin (MMP7), Insulin-like growth factor-binding protein 3 (IBP3), Insulin-like growth factor-binding protein 2 (IBP2), Vascular cell adhesion protein 1 (VCAM1), Connective tissue growth factor (CTGF), Syndecan-4 (SDC4), Aquaporin-2 (AQP2), Selenoprotein P (SEPP1), Urokinase plasminogen activator surface receptor (UPAR), Insulin-like growth factor-binding protein 7 (IBP7), Endothelial cell-selective adhesion molecule (ESAM), Cytosolic non-specific dipeptidase (CNDP2). Urine (0.2 mL) was supplemented with 1 µg of α-amylase from *Aspergillus oryzea*, which helps provide bulk protein to optimize protein precipitation and helps control for the variability in digestion from sample to sample. Ice-cold acidified methanol:acetone 50%:50% (v:v, 0.8 mL) was used to precipitate proteins for 24 h at -20°C. Precipitated proteins are dried under vacuum and then reconstituted in 0.5% sodium deoxycholate in 50 mM ammonium bicarbonate. Proteins were reduced in 5 mM dithiothreitol for 1 h at 60°C, alkylated in 15 mM iodoacetamide for 30 min at room temperature in the dark, and then digested with 1 µg trypsin (Worthington Biomedical, Lakewood, NJ) for 2 h at 37°C with shaking (Thermomixer, 1400 rpm). Deoxycholate was precipitated by the addition of HCl (final concentration of 200 mM), which was removed by centrifugation. The supernatant was desalted using solid phase extraction (HLB µElute plate, Waters, Milford, MA). The eluted peptides were dried under vacuum and reconstituted in 5% acetonitrile in 0.1% formic acid, which was then spiked with internal standard peptides. Proteins of interest were quantified using LC-MS/MS on a Thermo Orbitrap mass spectrometer coupled to an Easy-nLC liquid chromatography system (Thermo Scientific, Waltham, MA). Selected peptides from the proteins of interest were monitored by selecting their precursor ions in the isolation quadrupole (selection window 1.5 Da) and full scan MS/MS after HCD fragmentation (NCE 27) in the Orbitrap analyzer using the lowest resolution (17,500) setting to increase scan rate. Scheduled acquisition with five-minute acquisition windows were set up for each peptide precursor using Skyline software (*118*), allowing a maximum of 30 concurrent PRM experiments at any given time. Acquired data was then processed in Skyline and automated integration was

manually checked for each peptide chromatogram. Data Processing: Acquired data was then processed in Skyline and automated integration is manually checked for each peptide chromatogram.

Untargeted Urine Proteomics. The digested peptides (375 ng) were injected on a trap column (40 x 0.1 mm, Reprosil-Pur 120 C18-AQ, 5 um, Dr.Maisch GmbH, Germany), desalted for 5 min at a flow of 4 µL/min and separated on a pulled tip analytical column (250 x 0.075 mm, Reprosil-Pur 120 C18-AQ,, 5 um, Dr. Maisch GmbH, Germany) with a three-segment linear gradient of acetonitrile, 0.1%FA (B) in water,0.1%FA (A) as follows: 0-3 min 1-7%B, 3-53 min 7-25%B, 53-60 min 25-35%B followed by column wash at 80% B and reequilibration at a flow rate 0.4 uL/min (Waters NanoACQUITY UPLC). Analysis using the data independent acquisition was performed in two steps. A chromatogram library, peptide and protein identification and spectral library was performed with narrow mass window selection for the MS/MS (2 m/z) on a pooled sample. The study samples were analyzed with a wider mass window selection for MS/MS (10 m/z). The data independent analysis was performed on Orbitrap Fusion Lumos (Thermo Scientific) as follows: single full scan MS1 is acquired over m/z range 395-1005 at resolution 120,000 followed by 60 MS/MS spectra with a 10 m/z window selection stepped over the range 400-1000 with HCD fragmentation mode (NCE 30) and MSMS acquisition in the Orbitrap analyzer at resolution 17,500. For Chromatogram library generation a sample pooled across multiple subjects and timepoints was analyzed in a similar fashion in 6 separate injections with the DIA acquisition using 2 m/z window over m/z ranges 400-520, 520-640, 640-760, 760880, 880-1000. Data processing: A spectral library of identified peptides and proteins was generated using a pipeline combining two approaches – a combination of DIA Umpire to extract MS/MS spectra followed by a Comet database search, and a direct approach using PECAN (*119*) lemented in EncyclopeDIA (*120*) Proteins and peptides were then quantified in each sample using EncyclopeDIA and Skyline (*118, 120*) using with an mProphet probability scoring algorithm (http://mprophet.org) and are filtered at q-value=0.01 to generate list of quantifiable peptides and proteins together with corresponding quantitative responses. The data was further processed and quantified in Skyline and mapDIA (*121*) software packages. Individual protein and peptide responses were exported for further statistical analysis. Peak areas for each endogenous peptide were normalized to internal standard peptides from a stable isotope-labeled internal standard proteinthe α-amylase protein standard to generate a peak area ratio for each peptide in each sample. Peak area ratios for each protein were averaged, and protein peak area ratios then normalized to protein peak area ratios for calibrator samples included in each digestion batch. The resulting calibrated protein peak area ratios were used as relative concentrations of each protein.

Untargeted plasma proteomics. Plasma proteins were reduced by 5 mM tris(2-carboxyethyl)phosphine and alkylated using 10 mM iodoacetamide. They were then digested by trypsin using 1:20 protein ratio. Tryptic peptides of plasma samples were separated on a NanoLC™ 425 System (SCIEX). 5 ul/min flow was used with trap-elute setting using a 0.5 x 10 mm ChromXP™ (SCIEX). LC gradient was set to a 43-minute gradient from 4-32% B with 1 hour total run. Mobile phase A was 100% water with 0.1% formic acid. Mobile phase B was 100% acetonitrile with 0.1% formic acid. 8ug load of undepleted plasma on 15cm ChromXP column. MS analyses were performed using SWATH®Acquisition on a TripleTOF®6600 System equipped with a DuoSpray™Source and 25 µm I.D. electrode (SCIEX). Variable Q1 window SWATH Acquisition methods (100 windows) were built in high sensitivity MS/MS mode with Analyst®TF Software 1.7.

Peakgroups from individual runs were statistically scored with pyProphet and all runs were aligned using TRIC to produce a final data matrix. Protein abundances were computed as the sum of the three most abundant peptides (top3 method). After log-transformation and scaling by median count, a linear model was fit to the data. The false discovery rates (FDRs) were estimated using the "p.adjust" function in R. Proteins were considered discriminant when the adjusted p-value was below 0.05.

Cytokine assays. Levels of circulating cytokines in the blood were measured using a 63-plex Luminex antibody-conjugated bead capture assay (Affymetrix) that has been extensively characterized and benchmarked by the Stanford Human Immune Monitoring Center (HIMC). Human 63-plex kits were purchased from eBiosciences/Affymetrix and used according to the manufacturer's recommendations with modifications as described below. Briefly, beads were added to a 96-well plate and washed using a Biotek ELx405 washer. Samples were added to the plate containing the mixed antibody-linked beads and incubated at room temperature for 1 h followed by overnight incubation at 4 °C with shaking. Cold and room temperature incubation steps were performed on an orbital shaker at 500-600 rpm. Following the overnight incubation, plates were washed using a Biotek ELx405 washer and then biotinylated detection antibody added for 75 min at room temperature with shaking. The plate was washed as above and streptavidin-PE was added. After incubation for 30 min at room temperature, a wash was performed as above and reading buffer was added to the wells. Each sample was measured in duplicate. Plates were read using a Luminex 200 instrument with a lower bound of 50 beads per sample per cytokine. Custom assay control beads by Radix Biosolutions were added to all wells. After log-transformation and scaling by median count, linear models were fit to the data. The false discovery rates (FDRs) were estimated using the "p.adjust" function in R. Cytokines were considered discriminant when the adjusted p-value was below 0.05. Functional term enrichments were identified using the web-based tool DAVID (*122*).

Metabolomics

Targeted Urine and Plasma Metabolomics. Analysis were performed on plasma and 24 h urine samples on a gas chromatography coupled to tandem mass spectroscopy (GC-MS/MS). Tandem mass spectroscopy used in this analysis overcomes common limitations of multiple analytes of same molecular mass and retention time and endogenous matrix interference, thus allowing accurate identification and quantification in multiple reaction monitoring (MRM) mode. Approximately 80 organic acid metabolites were simultaneously analyzed and quantified using calibrations curves. The panel of metabolites have been previously linked to inborn errors of metabolism and correspond to 37 different metabolic pathways. Major pathways include TCA cycle, amino acid and fatty acid metabolism, ketone bodies, hypoxia and oxidative stress. Samples were randomized in excel and analyzed in a semi-blinded manner in a way that longitudinal samples corresponding to each subject were analyzed in the same batch to avoid batch variation. Urine samples were aliquoted into 500 ul volume and frozen at -80 °C. All analyses were carried out in samples that were limited to less than 3 freeze thaws. Prior to metabolomic analysis urine creatinine concentrations were determined using Creatinine assay kit from Cayman chemicals following manufacturer's protocol. For GC-MS analysis urine samples equivalent to 0.5 uM creatinine were combined with internal standard (IS) mix (mix of 10 heavy isotope labeled organic acids under analysis or structurally similar compounds) were derivatized with pentafluorobenzyl hydroxylamine to oximate ketoacids and lyophilized overnight. Subsequently, the organic acids were extracted by solid phase extraction on silica (42% 2methyl-2-butanol in chloroform) and dried under Nitrogen. The dry residue was silylated with 1:1 mix of Trisil + N,O-bis (trimethylsilyl) trifluoroacetamide at 60 °C for 2 h and 1 µL of the derivatized sample were injected using CP8400 liquid autosampler into a PTV injector maintained at 300 °C in a splitless mode. The compounds were separated onto a 20 m x 0.36 µm column (Agilent DB-5) at 80 °C in a gas chromatogram (Bruker Scion 436 GC) and eluted with helium gas at a temperature gradient of 80 to 300 ºC over 20 min. Following electron ionization target metabolites were analyzed by electron ionization on an E VOQ ScionTriple quadrupole mass spectrometer equipped with extended dynamic range detector. Each analyte was identified based on their MRM transitions and confirmed based on the ratios of qualifying and quantifying ions. Metabolite concentrations were calculated from calibration curves developed for each analyte using similar protocol with purified compounds. Metabolite peak areas were normalized to internal standard peak areas to adjust for technical variation. A pooled healthy urine or plasma sample was run after every 8 samples in each batch to be used as a control to adjust for instrument drift. For plasma metaobolomics, metabolites were

extracted from 200 µl of plasma samples that were deproteinated with 800 µl of acetonitrile. The organic layer was evaporated under nitrogen and derivatized as described above for urine samples.

Untargeted plasma metabolomics. Plasma metabolites were profiled using a broad-spectrum LC-MS platform as previously described (*18, 123*). Briefly, metabolites were extracted using 1:1:1 acetone:acetonitrile:methanol, evaporated to dryness under nitrogen and reconstituted in 1:1 methanol:water before analysis. Metabolic extracts were analyzed four times using HILIC and RPLC separation in both positive and negative ionization modes. Data were acquired on a Thermo Q Exactive plus mass spectrometer for HILIC and a Thermo Q Exactive mass spectrometer for RPLC. Both instruments were equipped with a HESI-II probe and operated in full MS scan mode. MS/MS data were acquired on pool samples consisting of an equimolar mixture of all the samples comprised in the study. HILIC experiments were performed using a ZIC-HILIC column 2.1 x 100 mm, 3.5 µm, 200Å (Merck Millipore) and mobile phase solvents consisting of 10 mM ammonium acetate in 50/50 acetonitrile/water (A) and 10 mM ammonium acetate in 95/5 acetonitrile/water (B). RPLC experiments were performed using a Zorbax SBaq column 2.1 x 132 50 mm, 1.7 µm, 100Å (Agilent Technologies) and mobile phase solvents consisting of 0.06% acetic acid in water (A) and 0.06% acetic acid in methanol (B). Data quality was ensured by (i) sample randomization for metabolite extraction and data acquisition, (ii) injection of 12 and 6 pool samples to equilibrate the LC-MS system prior to run the sequence for HILIC and RPLC respectively, (iii) injection of pool samples every 8-10 injections to control for signal deviation with time, (iv) discarding features from solvent blanks, (v) checking mass accuracy, retention time and peak shape of internal standards in every sample.

Untargeted LC-MS metabolomics data were processed using an in-house data analysis pipeline written in R (version 3.0.1). Metabolite features (characterized by a unique mass/charge ratio and retention time) were extracted, aligned and quantified with the "XCMS" package (version 1.39.4) after conversion of .RAW files to .mzXML using the ProteoWizard MS convert tool. Grouping and annotation were performed with the "CAMERA" package (version 1.16.0). Metabolic features from blanks and that didn't show sufficient linearity upon dilution were discarded. Only metabolic features present in >33% of the samples were kept for further analysis and missing values were imputed using the k-nearest neighbors method. MS signal variation was corrected using the LOESS normalization method on pool samples injected repetitively along the sequence. This resulted in 4,162 metabolic features. Of these, 719 metabolites were confidently identified by matching retention time and/or fragmentation spectra to an in-house database comprised of formally identified metabolites based on authentic standards and public repositories. After log-transformation and scaling by median count, a linear model was fit to the data. The false discovery rates (FDRs) were estimated using the "p.adjust" function in R. Metabolites were considered discriminant when the adjusted p-value was below 0.05.

Mitochondrial respiration assay

Oxygen consumption rates (OCR) from a monolayer of adherent L6 cells (rat skeletal muscle cell line purchased from ATCC Cat. # CRL-1458), was measured using the Seahorse XF96 analyzer. The L6 cells were seeded at 20,000 cells/well (passage 3-4) on a 96 well tissue culture plate (Seahorse Biosciences, North Billerica, MA, USA) 24 h before the OCR measurements. The intact cells were incubated at 37 ºC for 1 h with XF media supplemented with 10 mM glucose, 1 mM sodium pyruvate, 2 mM L-glutamine, pH 7.4. The bioenergetic profile was derived by acutely injecting ground twin or flight twin astronaut plasma (5%) through the first of the 4 injection ports followed by the modulators of the electron transport chain. We utilized Oligomycin (1 uM) to achieve maximal respiration through uncoupling and inhibition of complex I and III through Rotenone/Antimycin A (0.5 uM), a complex I inhibitor. The OCR was calculated by plotting the O_2 tension of the media as a function of time (pmol/min).

Measurement of circulating cell-free mtDNA

The frozen plasma was thawed at 37C for 5min and spun at 16000g for 10 minutes at 4C to remove cryo-precipitates. The volume of each plasma sample (0.250ml – 1.000ml) was brought up to 1ml using sterile, nuclease-free 1X phosphate buffered saline pH 7.4. Circulating cell-free nucleic acid (ccfNA) was extracted using the Qiamp Circulating Nucleic Acid kit (Qiagen, USA) following the manufacturer's protocol. ccfNA was extracted in 50ul AE buffer. Concentration and size distribution information was obtained by running 1ul of ccfNA on the Agilent Bioanalyzer using the High Sensitivity DNA chip (Agilent technologies, CA, USA). 15µL of plasma was then used for mitochondrial DNA quantitation. The levels of mitochondrial DNA in isolated plasma DNA were measured by SYBR Green dye-based qPCR assay using 7500 Real Time RCR systems (Applied Biosystems) (*124*). The primer sequences were as follows: human NADH dehydrogenase 1 gene (hu mtNd1): forward 5'-ATACCCATGGCCAACCTCCT-3', reverse 5'-GGGCCTTTGCGTAGTTGTAT-3' (*124*). Plasmid DNA with complementary DNA sequences for human mtDNA was obtained from ORIGENE (SC101172). Concentrations were converted to copy number using the formula; mol/gram×molecules/mol = molecules/gram, via a DNA copy number calculator (http://cels.uri.edu/gsc/cndna.html; University of Rhode Island Genomics and Sequencing Center). The thermal profile for detecting mtDNA was carried out as follows: an initiation step for 2 min at 50°C is followed by a first denaturation step for 10 min at 95°C and a further step consisting of 40 cycles for 15 s at 95°C and for 1 min at 60°C. MtDNA levels in all of the plasma analyses were expressed in copies per microliter of plasma based on the following calculation: c=Q x VDNA/VPCR x 1/Vext; where c is the concentration of DNA in plasma (copies/microliter plasma); Q is the quantity (copies) of DNA determined by the sequence detector in a PCR; VDNA is the total volume of plasma DNA solution obtained after extraction; VPCR is the volume of plasma DNA solution used for PCR; and Vext is the volume of plasma extracted.

Biochemical Profile

Blood and urine samples were collected, processed, and analyzed as previously described, with the exception of updating the cytokine measurement detection to the Magpix detection unit (*13, 47, 125, 126*). Dietary intake was estimated using a Food Frequency Questionnaire completed once weekly during flight (*127, 128*). Body mass was determined as previously described (*46*).

Fluid Shifts Measures

Optical Coherence Tomography. Optical coherence tomography (Spectralis HRA + OCT (Heidelberg Engineering, Heidelberg, Germany) was used to quantify optic nerve head tissue thickness and subfoveal choroid thickness before, during, and after spaceflight. The detailed methods to acquire and calculate choroid thickness measures have been previously discussed (*129*). Briefly, the OCT camera was mounted on a surgical arm to acquire images in the seated and supine postures, and an OCT camera was flown to the ISS.

Ultrasound. Sonographic measurements were obtained using a standard ultrasound device (VividQ, GE Healthcare). Pre- and postflight measures were acquired by a trained sonographer. Inflight measures were obtained by the astronaut using remote guidance, a real-time two-way communication method with which the astronaut is guided through image acquisition by an expert sonographer on the ground. Ultrasound images of the internal jugular vein were obtained to quantify venous congestion due to the headward fluid shift. The left internal jugular artery was imaged just below the confluence of the internal

jugular vein and the facial vein. Images were acquired at the end of quiet expiration. Forehead (midline) soft tissue thickness was measured to quantify fluid filtration into the tissue. Measurements at each site were obtained using a 12-5 MHz linear array transducer. All images were stored in triplicate for offline analysis using a custom software package (MatLab, MathWorks, Austin, TX). Images were analyzed by two trained sonographers blinded to each other's results. If their results differed by more than 10%, a third sonographer analyzed the images. Measurements for images passing these quality assurance standards were averaged across sonographers.

Carotid Artery Measurements

In TW, data were acquired in the laboratory at 163 and 72 days before launch, during spaceflight on the ISS at flight days 13, 74, 181, 238, 299, and 332, and 4 days after landing (see **Table S1** for details). Pre- and postflight data collection consisted of ultrasound measurements from the carotid artery acquired by a trained sonographer as well as biomarkers measured in a single, fasted blood draw and in a urine sample from a 48-h pool. Inflight measurements were similar to ground-based data except that urine samples were drawn from a 24-h pool, and ultrasound images were acquired by the astronaut through remote guidance, a real-time two-way communication system with which the astronaut is guided through image acquisition by an expert sonographer on the ground. The same measurements were acquired from the ground-based twin at dates corresponding to the 66 days before launch (GD-66), at 190 d of flight for TW (GD 190), and 2 days after landing (GD+2).

Pre-, in-, and postflight ultrasound images were acquired using standard sonography techniques (ASE standards) using a commercially-available ultrasound system (VividQ, GE Healthcare). All images were stored in triplicate for offline analysis using a custom software package (MatLab, MathWorks, Austin, TX). Images were analyzed by two trained sonographers blinded to each other's results. If their results differed by more than 10%, a third sonographer analyzed the images. Measurements for images passing these quality assurance standards were averaged across sonographers. During the first testing session in the laboratory, the sonographers determined the location for probe placement to acquire the best possible image and measured the distance from the earlobe to the top of the ultrasound probe. This distance was used in subsequent data collection sessions to determine probe location for consistency of anatomical measures.

Intima-media thickness was defined as the distance from the lumen of the vessel to the border between the media and adventitia. Only the far wall intima-media thickness was measured. Arterial diameter was defined as the distance from the near to the far wall border between media and adventitia and was measured during diastole (smallest diameter) and systole (largest diameter). Diastolic and systolic diameters were used to calculated arterial stiffness and compliance using accepted equations.

Cognition Assays

The computerized *Cognition* battery contains a subset of tests from a widely used and validated neurocognitive battery, the Penn Computerized Neurocognitive Battery (CNB) (*130-132*) emphasizing cognitive domains of particular interest in spaceflight (executive function, spatial orientation, emotion recognition) as well as a number of additional tests that have either been used extensively in spaceflight (*133, 134*) or that assess other spaceflight critical functions. The 10 Cognition tests were modified to reflect the high aptitude and motivation of astronauts. These tests assess a range of cognitive domains, and the brain regions primarily recruited by each test have been previously established (*52, 135*). *Cognition* has been validated in both astronauts and astronaut surrogate populations (*52, 136*). A detailed overview of the

computerized *Cognition* battery can be found in Basner et al. (*52*). Here, we provide a brief description of each test (modified from (*52*), see **Fig. 10A** for screenshots).

Motor Praxis (MP) Task. The MP task (*137*) was administered at the start of testing to ensure that participants have sufficient command of the computer interface, and immediately thereafter as a measure of sensorimotor speed. Participants were instructed to click on squares that appear randomly on the screen, with each successive square smaller and thus more difficult to track.

Visual Object Learning Test (VOLT). The VOLT assessed participant memory for complex figures (*138*). Participants were asked to memorize 10 sequentially displayed three-dimensional figures. Later, they were instructed to select those objects they memorized from a set of 20 such objects also sequentially presented, half of them from the learning set and half of them new.

Fractal 2-Back (F2B) Test. The F2B test (*139*) is a nonverbal variant of the Letter 2-Back. N-back tasks have become standard probes of the working memory system and activate canonical working memory brain areas. The F2B test consisted of the sequential presentation of a set of figures (fractals), each potentially repeated multiple times. Participants were instructed to respond when the current stimulus matched the stimulus displayed two figures ago. The current implementation used 62 consecutive stimuli.

Abstract Matching (AM) Test. The AM test (*140*) is a validated measure of the abstraction and flexibility components of executive function, including an ability to discern general rules from specific instances. The test paradigm presented subjects with two pairs of objects at the bottom left and right of the screen, varied on perceptual dimensions (e.g., color and shape). Subjects were presented with a target object in the upper middle of the screen that they had to classify as belonging more with one of the two pairs, based on a set of implicit, abstract rules. The current implementation used 30 consecutive stimuli.

Line Orientation Test (LOT). The LOT is a measure of spatial orientation that is derived from the well-validated Judgment of Line Orientation Test (*141*). The LOT format consisted of presenting two lines at a time, one stationary while the other could be rotated by clicking an arrow. Participants could rotate the movable line until they perceived it to be parallel to the stationary line. The implementation used in this study had 12 consecutive line pairs that varied in length and orientation.

Emotion Recognition Task (ERT). The ERT (*131*) is a measure of emotion identification. It presented subjects with photographs of professional actors (adults of varying age and ethnicity) portraying emotional facial expressions of varying types and intensities (biased towards lower intensities, and with the prevalence of emotion categories balanced within each version of the test). Subjects were given a set of emotion labels ("happy"; "sad"; "angry"; "fearful"; and "no emotion") and had to select the label that best described the expressed emotion. The implementation in the study used 40 consecutive stimuli, with eight stimuli each representing one of the above five emotion categories.

Matrix Reasoning Test (MRT). The MRT is a measure of abstract reasoning and consists of increasingly difficult pattern matching tasks (*137*). It is based on a well-known measure of general intelligence, the Raven Progressive Matrices (*142*) and recruits prefrontal, parietal, and temporal cortices (*143*). The test consisted of a series of patterns, overlaid on a grid. One element from the grid was missing and the participant had to select the element that fit the pattern from a set of alternative options. The implementation used in the study employed 12 consecutive stimuli.

Digit-Symbol Substitution Task (DSST). The DSST (*133*) is a computerized adaptation of a paradigm used in the Wechsler Adult Intelligence Scale (WAIS-III). The DSST required the participant to refer to a displayed legend relating each of the digits one through nine to specific symbols. One of the nine symbols

appeared on the screen and the participant had to select the corresponding number as quickly as possible. The test duration was fixed at 90 s, and the legend key was randomly reassigned with each administration.

Balloon Analog Risk Test (BART). The BART is a validated assessment of risk taking behavior (*144*). The BART required participants to either inflate an animated balloon or stop inflating and collect a reward. Participants were rewarded in proportion to the final size of each balloon, but a balloon popped after a hidden number of pumps, which changed across stimuli (*144*). The implementation used in the study had 30 consecutive stimuli. The average tendency of balloons to pop was systematically varied between test administrations. This required the subjects to adjust the level of risk based on the behavior of the balloons. It prevented subjects from identifying a strategy during the first administrations of the battery and carrying it through to later administrations.

Psychomotor Vigilance Test (PVT). The PVT records reaction times (RT) to visual stimuli that occur at random inter-stimulus intervals (*145*). Subjects were instructed to monitor a box on the screen, and press the spacebar once a millisecond counter appears in the box and starts incrementing. The reaction time was then displayed for one second. Subjects were instructed to be as fast as possible without hitting the spacebar in the absence of a stimulus (i.e., false starts or errors of commission). The PVT is a sensitive measure of vigilant attention, and has been well-established as a tool to detect acute and chronic sleep deprivation and circadian misalignment, conditions highly prevalent in spaceflight (*146*). The PVT has negligible aptitude and learning effects (*147*), and is ecologically relevant as sustained attention deficits and slow reactions affect many real-world tasks (e.g., operating a moving vehicle) (*148*). In the current study, the *Cognition* battery contained a validated 3 min brief PVT-B with 2-5 s inter-stimulus intervals and a 355 ms lapse threshold (*145*).

Both twins first watched a 30 min standardized familiarization video with the opportunity to ask questions afterwards. They then performed a first familiarization test bout on laptop computers calibrated for timing accuracy (ground model: Dell E5420; inflight model: Lenovo T61p). Both twins performed the Cognition battery 4 times preflight (including familiarization), 11 times inflight, and 3 times postflight (**Table S1**). Cognition administration was synchronized with blood draws whenever possible.

Analyses concentrated on one main accuracy and one main speed outcome for each Cognition test. For most tests, the standard accuracy outcome was "percent correct" and the standard speed outcome was "average response time across all stimuli" (i.e., including correct responses, incorrect responses, and timeouts). All accuracy outcomes ranged from 0% to 100% with 100% representing best possible performance. For all speed outcomes, lower values reflect shorter response times and thus higher speed. For the PVT, we used a reciprocal transform of response time (1/RT) and subtracted it from 10 so that higher values also reflected lower response speed.

For the MP, the distance from the center of each square (in pixels) was averaged across all responses. The center of the square translates to 100% accuracy, 50 pixels or more away from the center translate to an accuracy score of 0%, with linear scaling between zero and 50 pixels. For the LOT, the accuracy measure was calculated as three minus the average number of clicks off, which was then divided by three. For tests with more than three clicks off on average, the accuracy score was set to 0%. The BART risk score was based on empirical data of a normative cohort of subjects, with a value of 100% and 0% representing maximum and minimum risk-taking propensity. Here, we list BART risk-taking as an "accuracy" outcome despite the fact that it inherently measures risk taking. For the PVT, the accuracy score was calculated as 1 – [(# of Lapses + # of False Starts)/(Number of Stimuli + # of False Starts)]. Any response time not falling in-between the false start threshold (100 ms) and the lapse threshold (355 ms) thus decreased accuracy on the PVT.

One preflight VOLT administration and two inflight ERT administrations (both in the second half of the mission) were excluded from data analysis for TW as the data indicated a high likelihood of non-compliance (very fast responses paired with very low accuracy). Cognition data were corrected for practice and stimulus set difficulty effects based on findings from a study in 46 subjects that was designed to disentangle these effects that typically confound each other (results for the PVT reported in (*147*)). The data were also standardized relative to normative ground data from 15 astronauts (including TW and HR). Summary scores for accuracy and speed were calculated by averaging across z-transformed scores within the accuracy and speed domains, respectively. Due to its unique concept, the BART risk score was not included in the accuracy summary score. Speed summary scores were multiplied by -1 so that higher scores reflected higher speed. An efficiency score was calculated by averaging the accuracy and speed summary scores. Mixed effect models with random subject intercept were used for comparing TW's standardized performance scores with HR's standardized performance scores during four mission phases: preflight, early inflight (months 1-6), late inflight (months 7-12), and postflight.

Microbiome/Metagenome

Sample collections. All stool samples were swabbed within 2 h of voiding (see **Table S1** for collection details), using Hardy Diagnostics Envirotrans(TM) Swab Rinse Kit (sterile swab and test tube with 5 ml 0.85% saline; Cat # SRK35). Swabs were frozen and stored at -80ºC until extraction. The BiOstic Bacteremia DNA Isolation Kit (Qiagen, Mo Bio Laboratories, Inc.) was used to extract genomic DNA (gDNA) from 2 ml of sample in saline suspension, according to the manufacturer's directions. After inspection for genomic DNA quality (performed using a Qubit Spectrophotometer (Life Technologies, Grand Island, NY) and a TapeStation2200 (Agilent Technologies, Santa Clara, CA), gDNA was sheared using an acoustic device (Covaris S2, Covaris, Woburn, MA). DNA libraries for Illumina sequencers were made using the Accel-NGS 1S Plus DNA Library Kit (Swift Biosciences, Inc., Ann Arbor, MI). Libraries were pooled and sequenced on an Illumina MiniSeq sequencer and, based on the relative abundance of reads generated, were re-pooled and then sequenced on a high-output 300 cycle kit run on an Illumina NextSeq500 sequencer. Swabs were processed at Northwestern University, and library preparation and sequencing was performed at the DNA Services Facility, Research Resources Center, at the University of Illinois at Chicago. Sequencing statistics are included in **Table S10**.

Taxonomic and functional profiling. Raw reads were mapped to the NCBI non-redundant protein database using the software package DIAMOND (*149*). Taxonomic summaries per read were obtained using MEGAN's Least Common Ancestor algorithm (*150*), and then summarized across all reads to create counts per taxon. Raw counts were normalized to percentages for relative abundance. Functional profiling was performed using SUPER-FOCUS (*151*), with parameters "-a diamond -db DB_100 -n 0". Raw counts were normalized to percentages for relative abundance. Alpha diversity calculations, ordination plot visualization, and calculations of analysis of similarity (ANOSIM) were performed with the software package Primer7 (PRIMER-E Ltd, Plymouth, UK).

Differential analysis. Differential statistics were computed using edgeR (*152, 153*) on raw counts obtained from quantification (species-level for taxonomy, all SEED functions for functional). Multi-group p-values were computed to identify differences in relative abundance between preflight, flight, and postflight sample groups for the flight twin (TW). All significance values were corrected for multiple testing using the false discovery rate (FDR) correction method of Benjamini and Hochberg (*154*). Significantly differential abundant taxa and functional groups were identified as those with FDR < 0.05.

Multi-omics Analyses

The processed datasets (described above) for RNA-Seq (gene counts from CPT-frozen blood only), protein abundances from SWATH proteomics, quantified metabolic features from untargeted metabolomics, abundances from the cytokine immunoassays, read count data from species-level microbiome profiling, quantitative results from the cognition battery assays and telomere qPCR data were compiled and all analyte values were centered and scaled (R function "scale"). The resulting scaled multi-omic matrices were then used as input for fuzzy c-means soft longitudinal clustering analysis (R package "mfuzz") (*155*). Clustering was performed on all timepoints for the flight participant, and the profiles for all analytes in each cluster were then compared to that of the ground participant to look for divergent trends. Biological significance of the identified clusters was determined for the associated analytes using the integrated pathway analysis tool IMPaLA (pathway over-representation analysis function) (*156*), using as input official gene symbols for transcriptomic or proteomic data and putative associated KEGG identifiers for metabolomic features. Due to the overabundance of transcriptomic features versus those from the other 'omics data, clustering was performed with and without the RNA-seq dataset. For the larger dataset including RNA-seq, 30 clusters were generated, while eight clusters were specified for the smaller dataset excluding RNA-seq.

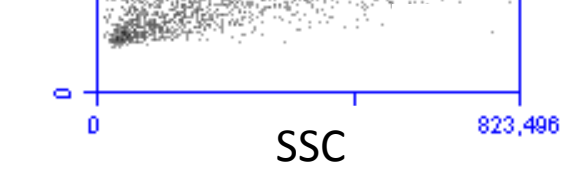
0
SSC
823,496

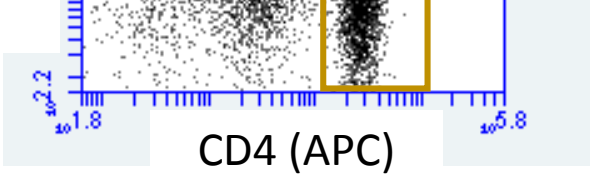
CD4 (APC)

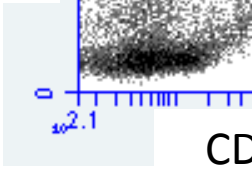

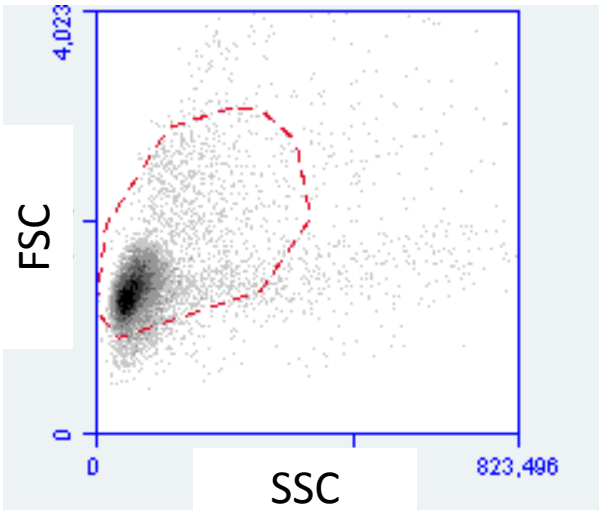
4,023
FSC
0
SSC
823,496

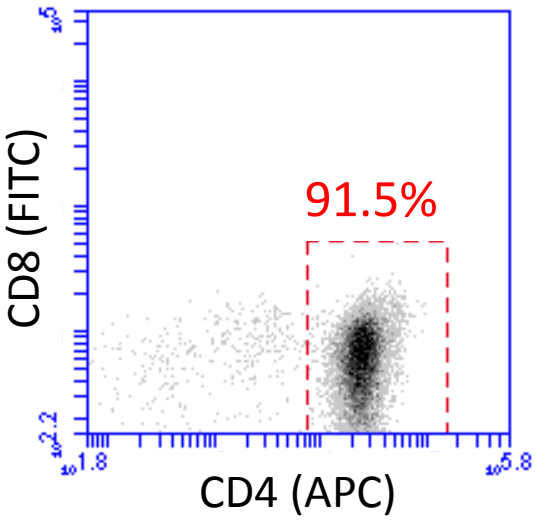
CD8 (FITC)
91.5%
CD4 (APC)

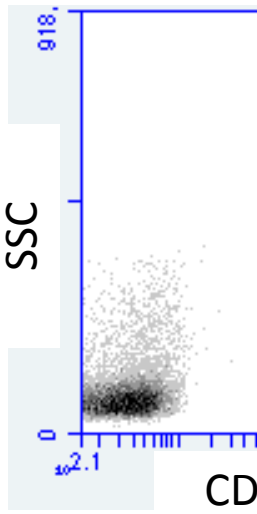
SSC

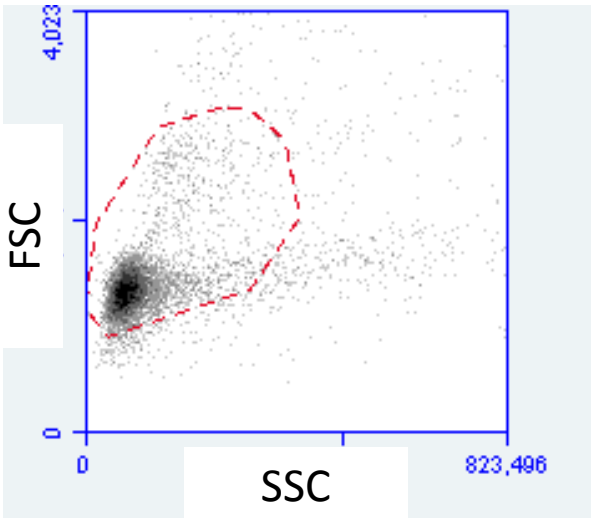
4,023
FSC
0
SSC
823,496

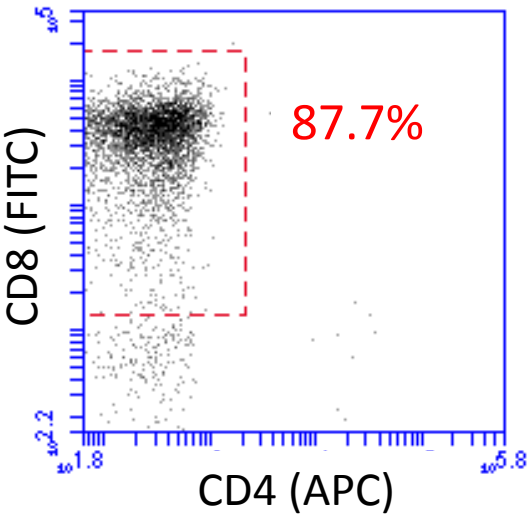
CD8 (FITC)
87.7%
CD4 (APC)

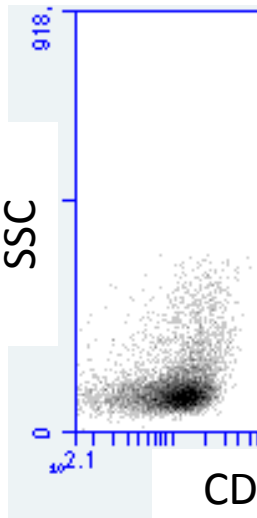
SSC

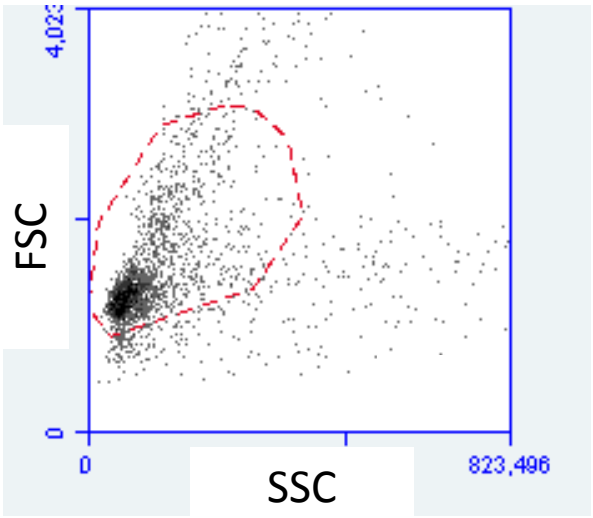
FSC
0
SSC
823,496

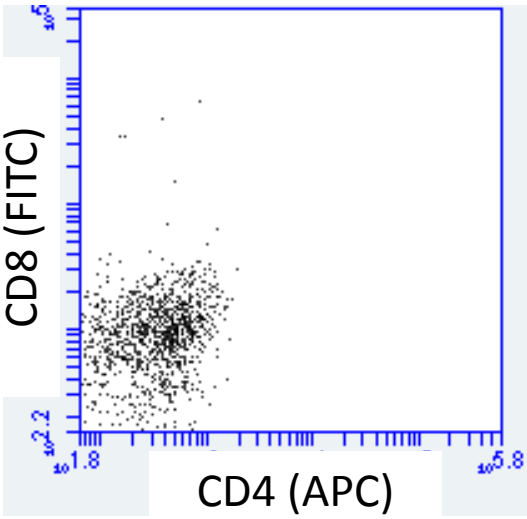
CD8 (FITC)
CD4 (APC)

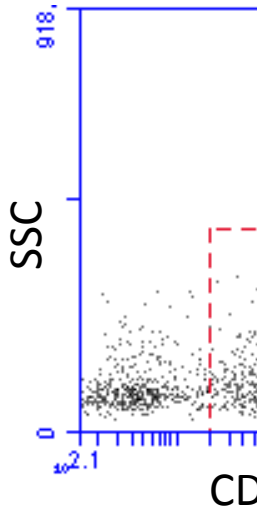
SSC

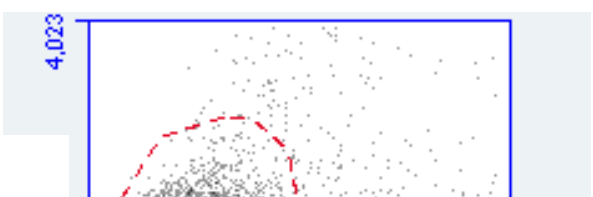
4,023

Fig. S1

Validation of cell separation and purification approach from CPT vacutainers. Four mL of human blood (healthy test subject) was collected into a CPT vacutainer and subjected to cell separation as described for fresh collections. Cell purity was assessed with flow cytometry on an Accuri flow cytometer (BD biosciences). Representative bivariate flow cytometry dot plots are presented for: (A) resolution and gating of peripheral blood mononuclear cells derived from the CPT density gradient centrifugation process by scatter properties; (B) CD4-selected cells (91% purity); (C) CD8-selected cells (88% purity); (D) CD19-selected cells (72% purity); (E) Flow through cells (Lymphocyte Depleted; LD). For analysis of lymphocyte subsets by fluorescence, PBMC were 'gated' as illustrated in the left plot for each analysis, and gated PBMC were plotted for fluorescence for detection of T cell subsets (center figure) or B cells (right figure). Antibodies used were purchased from Beckman-Coulter (Miami, Florida): CD8-FITC (clone BW135/80), CD19-PE (clone: LT19) and CD4-APC (clone: M-T466).

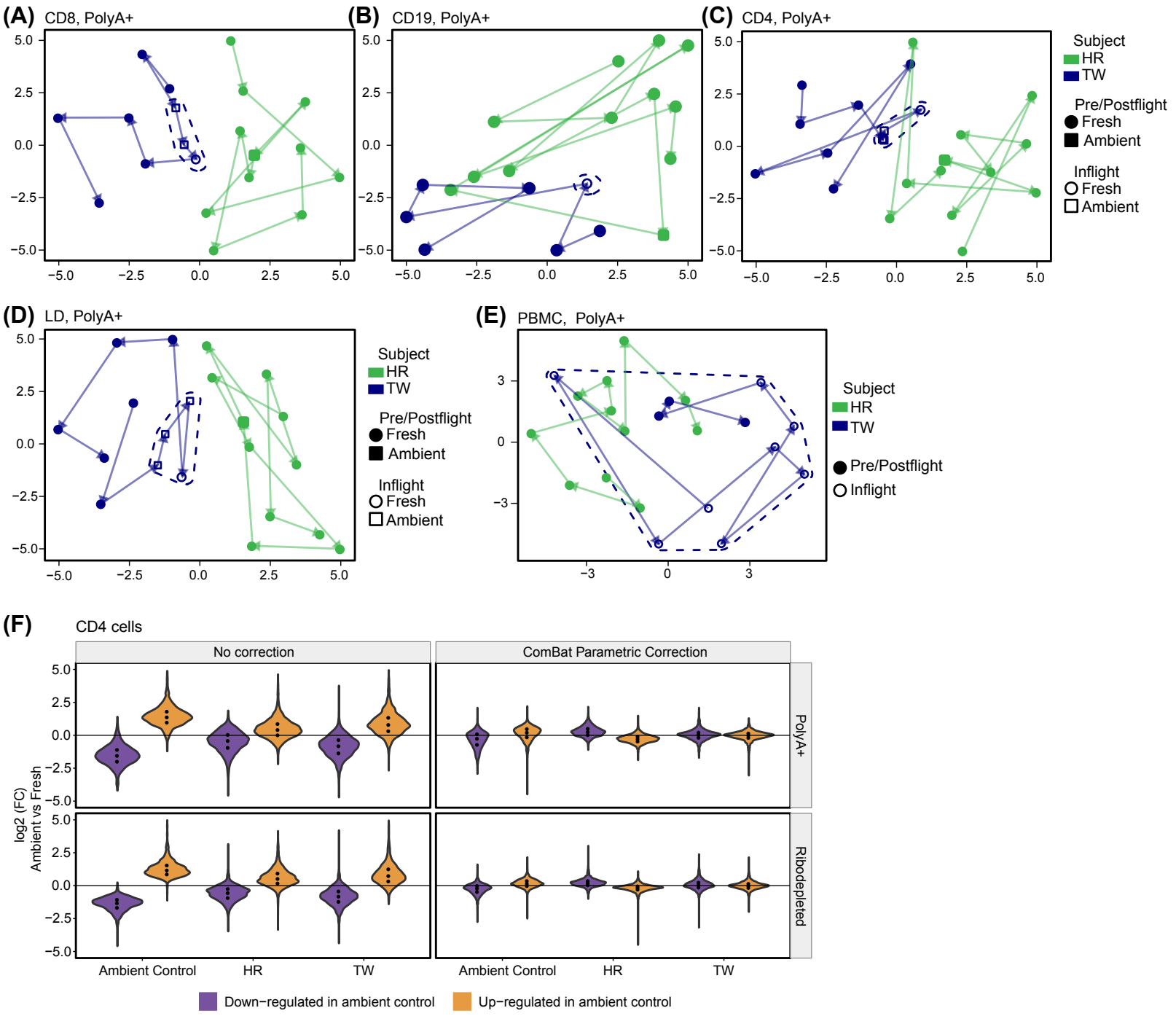
(A) CD8, PolyA+
(B) CD19, PolyA+
(C) CD4, PolyA+
Subject
HR
TW
Pre/Postflight
Fresh
Ambient
Inflight
Fresh
Ambient
(D) LD, PolyA+
(E) PBMC, PolyA+
(F) CD4 cells
No correction
ComBat Parametric Correction
PolyA+
Ribodepleted
log2 (FC)
Ambient vs Fresh
Ambient Control
HR
TW
Down−regulated in ambient control
Up−regulated in ambient control

Fig. S2

Global gene expression differences. 2-dimensional embedding of the expression data for **(A)** CD8, **(B)** CD19, and **(C)** CD4 cells as well as **(D)** lymphocyte depleted (LD) and **(E)** PBMCs in PolyA+ selection. Each point represents one time point for HR (green) and TW (blue), arrows between points show chronological order of samples. Samples taken inflight are shown as empty points and circled with dashed lines for emphasis, ground based samples are shown as filled. For sorted cell populations the samples that were returned on ambient temperature are shown as squares whereas circles represent fresh (in sorted cells) or frozen (in unsorted PBMCs). TMM normalized log(FPKM) values were corrected for ambient return related effects using ComBat and dimensionality reduction was performed using t-SNE (t-statistic distributed stochastic neighbor embedding). **(F)** Effect of ambient return on gene expression signature and correction by ComBat. Differentially expressed genes due to ambient return were calculated by comparing freshly processed and simulated ambient return samples. Log_2 fold-change values of difference between ambient and fresh pairs for the control sample, HR and TW are plotted for the same genes that are either up- or down-regulated in the ambient control. Left panel contains the normalized uncorrected expression values, right panel shows the same data after correcting all samples by ComBat to reduce the effects of ambient return bias.

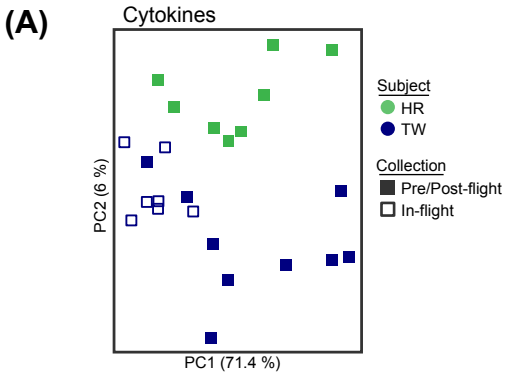
(A)
Cytokines
Subject
HR
TW
Collection
Pre/Post-flight
In-flight
PC2 (6 %)
PC1 (71.4 %)

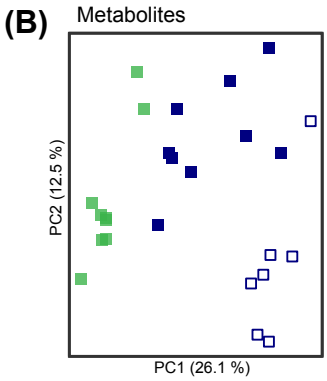
(B)
Metabolites
PC2 (12.5 %)
PC1 (26.1 %)

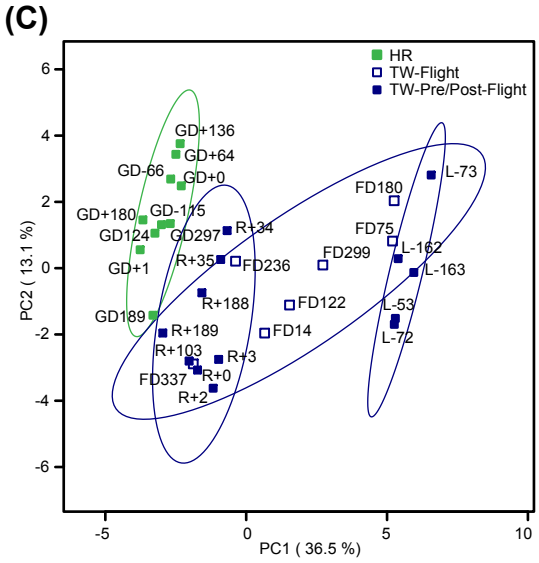
(C)
HR
TW-Flight
TW-Pre/Post-Flight
PC2 (13.1 %)
PC1 (36.5 %)

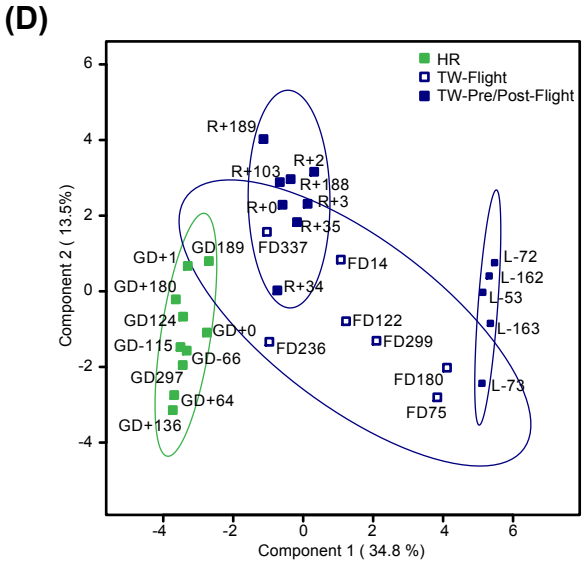
(D)
HR
TW-Flight
TW-Pre/Post-Flight
Component 2 (13.5%)
Component 1 (34.8 %)

Fig. S3

Global view of metabolome and cytokine profiles. Exploratory analysis of global cytokine (in **A**), metabolome (in **B**), and targeted urine metabolome (in **C**) profiles for HR (green) and TW (blue), using Principal Components Analysis. **(D)** Same data as in C analyzed using Partial Least Squares - Discriminant Analysis (PLS-DA). Filled squares represent samples collected on ground, whereas empty squares indicate samples collected inflight, aboard the ISS. Each principal component is labeled with % variance explained.

A) Fluid Regulation

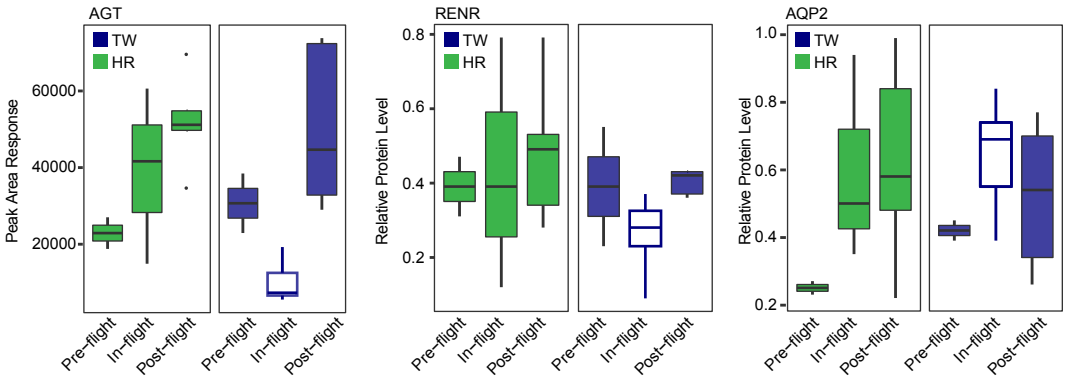

B) Vascular Remodeling

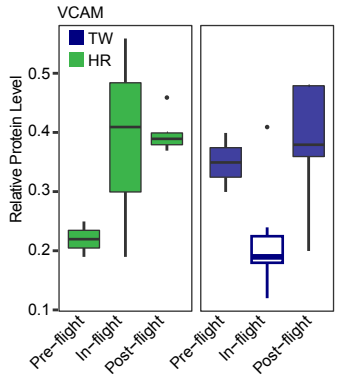

C) Musculoskeletal Deconditioning

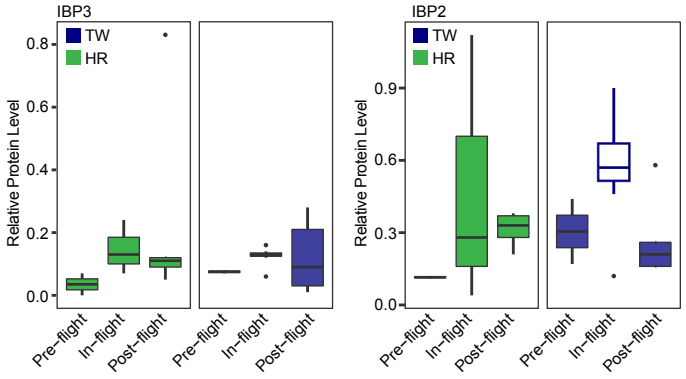

D) Extracellular Matrix

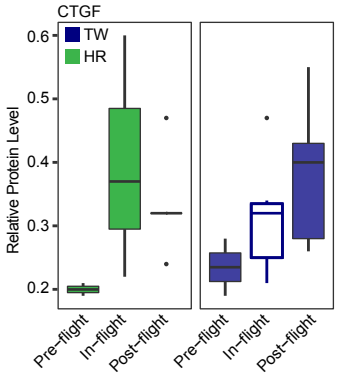

Fig. S4

Proteomic changes in urine during spaceflight. Liquid-chromatography coupled to tandem mass spectrometry (LC-MS/MS) was used for targeted and untargeted proteomic analysis of urine. Relative levels of peptides associated with **(A)** fluid regulation, **(B)** vascular remodeling, **(C)** musculoskeletal deconditioning and **(D)** extracellular matrix differed during spaceflight compared to ground time points.

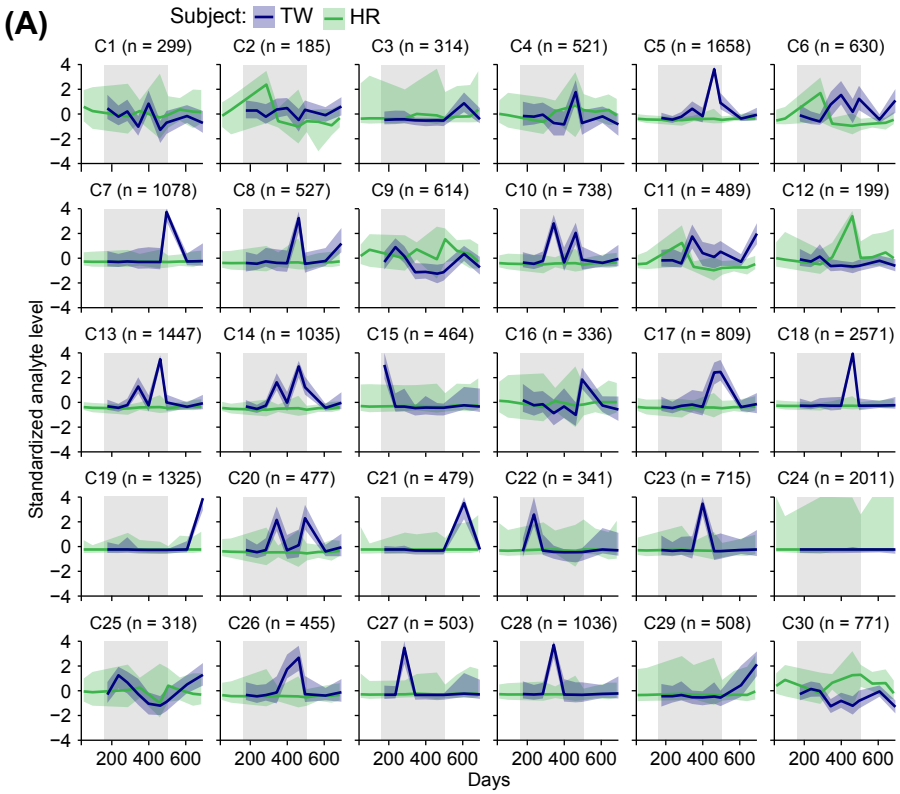
(A)
Subject: TW HR
C1 (n = 299)
C2 (n = 185)
C3 (n = 314)
C4 (n = 521)
C5 (n = 1658)
C6 (n = 630)
C7 (n = 1078)
C8 (n = 527)
C9 (n = 614)
C10 (n = 738)
C11 (n = 489)
C12 (n = 199)
C13 (n = 1447)
C14 (n = 1035)
C15 (n = 464)
C16 (n = 336)
C17 (n = 809)
C18 (n = 2571)
C19 (n = 1325)
C20 (n = 477)
C21 (n = 479)
C22 (n = 341)
C23 (n = 715)
C24 (n = 2011)
C25 (n = 318)
C26 (n = 455)
C27 (n = 503)
C28 (n = 1036)
C29 (n = 508)
C30 (n = 771)
Standardized analyte level
Days

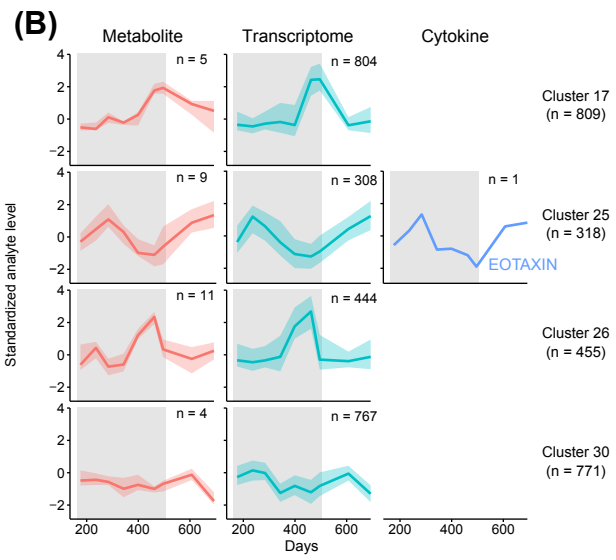
(B)
Metabolite
Transcriptome
Cytokine
n = 5
n = 804
n = 9
n = 308
n = 1
EOTAXIN
n = 11
n = 444
n = 4
n = 767
Cluster 17 (n = 809)
Cluster 25 (n = 318)
Cluster 26 (n = 455)
Cluster 30 (n = 771)
Standardized analyte level
Days

Fig. S5

Integrative analysis of multi-omic data including RNA-seq. The results of longitudinal c-means clustering are shown for RNA-seq, proteomics, metabolomics and cytokine data. **(A)** Changes in analyte abundance (scaled) over time during the mission are indicated for analytes in the identified thirty clusters. **(B)** A subset of spaceflight-relevant clusters are shown with each analyte type plotted separately. In both panels, bold line indicates median abundance within a cluster. Shaded area ribbons indicate the 5th and 95th percentile of abundance.

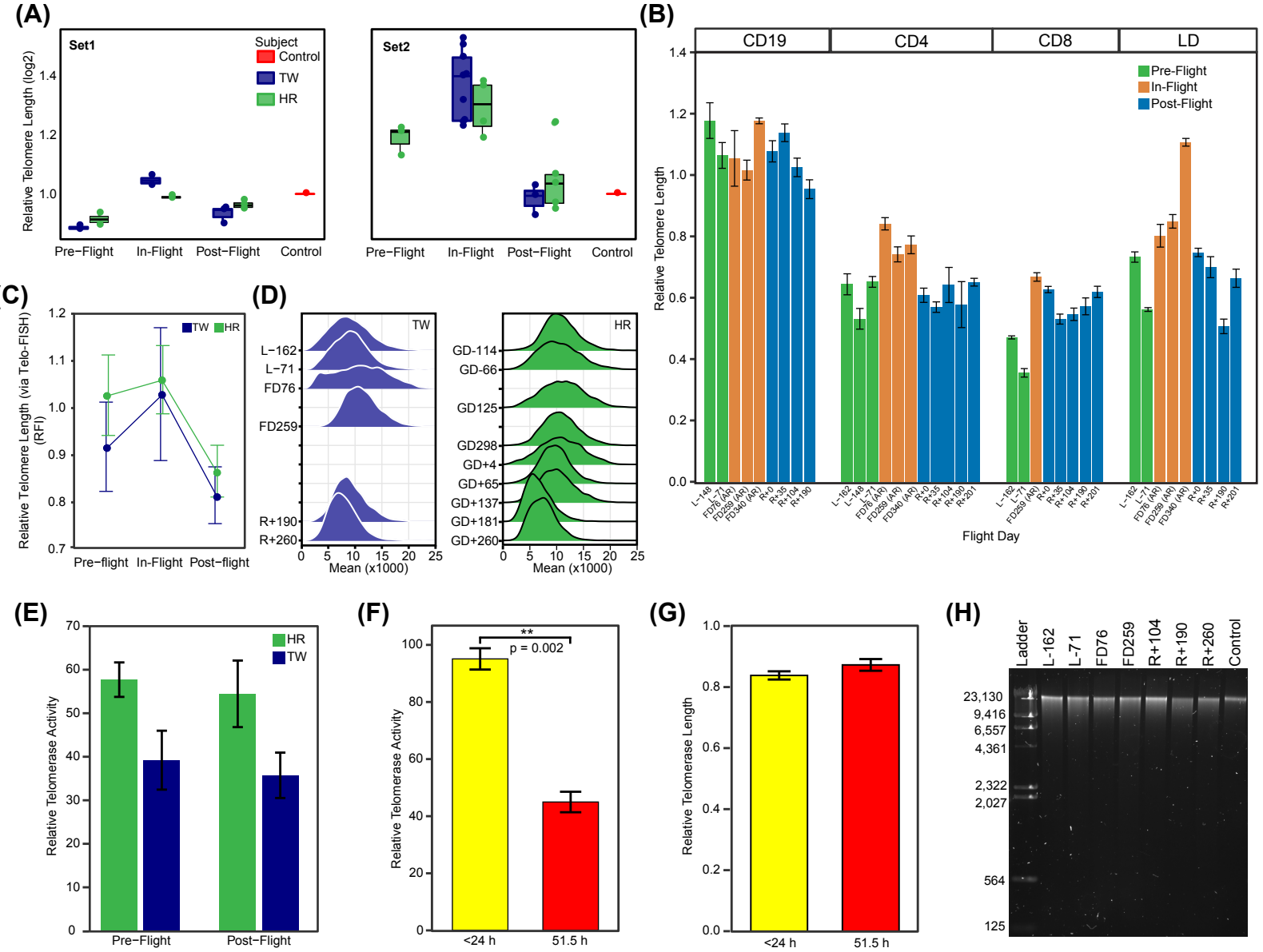
(A)
Set1
Set2
Subject
Control
TW
HR
Relative Telomere Length (log2)
Pre−Flight
In−Flight
Post−Flight
Control
(B)
CD19
CD4
CD8
LD
Pre-Flight
In-Flight
Post-Flight
Relative Telomere Length
Flight Day
(C)
TW
HR
Relative Telomere Length (via Telo-FISH) (RFI)
Pre−flight
In-Flight
Post−flight
(D)
L−162
L−71
FD76
FD259
R+190
R+260
GD-114
GD-66
GD125
GD298
GD+4
GD+65
GD+137
GD+181
GD+260
Mean (x1000)
(E)
HR
TW
Relative Telomerase Activity
Pre−Flight
Post−Flight
(F)
p = 0.002
Relative Telomerase Activity
<24 h
51.5 h
(G)
Relative Telomerase Length
<24 h
51.5 h
(H)
Ladder
L-162
L-71
FD76
FD259
R+104
R+190
R+260
Control
23,130
9,416
6,557
4,361
2,322
2,027
564
125

Fig. S6

Telomere length dynamics and telomerase activity. (A) Relative average telomere length for TW (blue) and HR (green) pre-, in-, and postflight, evaluated via qRT-PCR in DNA isolated from PBMCs collected by Colorado State University (CSU) (Set1) and Cornell (Set2). All samples were normalized to a human genomic DNA control (red), and data was $\log_2$ transformed to account for inter-laboratory variation. **(B)** Relative average telomere length for TW pre-, in-, and postflight, evaluated via qRT-PCR in DNA isolated from sorted PBMC subpopulations; CD4 and CD8 T-cells, CD19 B-cells, and lymphocyte depleted (LD) fractions. Data correspond to that shown in Figure 2b; individual time points shown. Error bars represent SEM. **(C)** Telo-FISH cell-by-cell analysis of average telomere length (relative fluorescence intensity; RFI) on metaphase chromosomes (PHA stimulated T-cells) pre-, in-, and postflight; inflight differences were not statistically significant (one-way ANOVA). Error bars represent SEM. **(D)** Telo-FISH generated histograms of individual telomere length distributions for TW (blue) and HR (green) pre-, in-, and postflight. Data correspond to selected distributions depicted in Figure 2 (C,D); individual time points shown. **(E)** Telomerase activity in PBMCs determined using qRT-PCR TRAP. **(F,G)** Influence of transit time on telomerase activity (in **F**) and telomere length (in **G**) for blood samples in transit < 24 h, and > 48 h, prior to processing at CSU; one control sample each, run in triplicate. **(H)** Gel confirming no degradation of DNA in mid-flight samples that underwent ambient return from the ISS. Significance tested by a student's t-test. All error bars represent SEM.

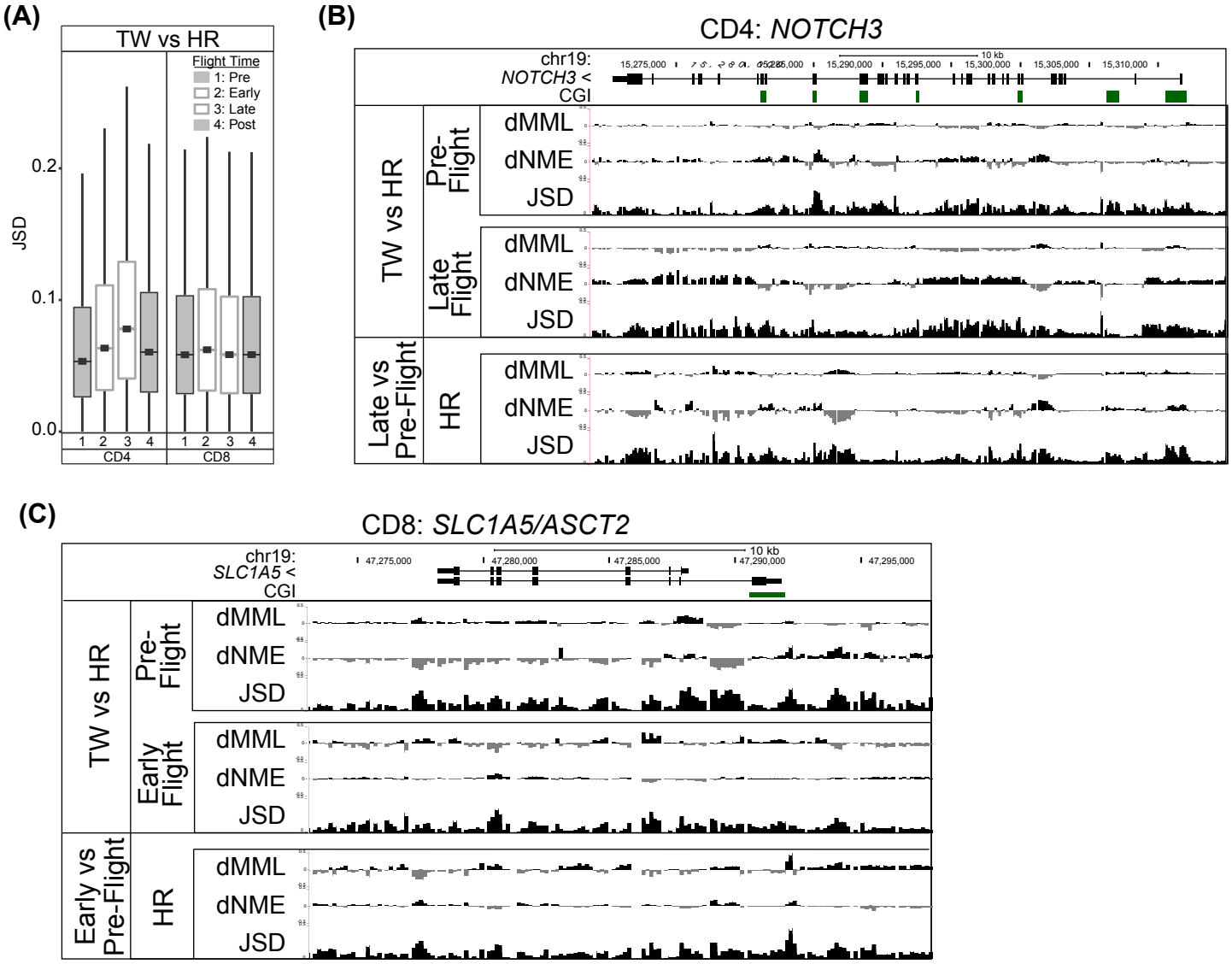
(A)
TW vs HR
Flight Time
1: Pre
2: Early
3: Late
4: Post
JSD
0.2
0.1
0.0
1 2 3 4
1 2 3 4
CD4
CD8
(B)
CD4: NOTCH3
chr19:
NOTCH3 <
CGI
15,275,000
15,285,000
15,290,000
15,295,000
15,300,000
15,305,000
15,310,000
10 kb
TW vs HR
Pre-Flight
Late Flight
Late vs Pre-Flight
HR
dMML
dNME
JSD
(C)
CD8: SLC1A5/ASCT2
chr19:
SLC1A5 <
CGI
47,275,000
47,280,000
47,285,000
47,290,000
47,295,000
10 kb
TW vs HR
Pre-Flight
Early Flight
Early vs Pre-Flight
HR
dMML
dNME
JSD

Fig. S7

DNA methylation dynamics during spaceflight. (A) Genome-wide distributions of Jensen-Shannon distances (JSD) comparing TW to HR within CD4 and CD8 T-cells. Center lines, median; boxes, interquartile range (IQR); whiskers, 1.5 × IQR. **(B,C)** UCSC genome browser images of example genes for the indicated comparisons in CD4 (in **B**) or CD8 (in **C**) cells. Comparisons include: TW versus HR at preflight and inflight time points (**B**, FD259; **C**, FD76), and HR at inflight (**B**, FD259; **C**, FD76) versus preflight time points. Peaks of Jensen-Shannon distances (JSD) are plotted along with differential MML (dMML) and differential NME (dNME) with negative values indicating reduced MML or NME at the inflight time point compared to preflight or in TW compared to HR.

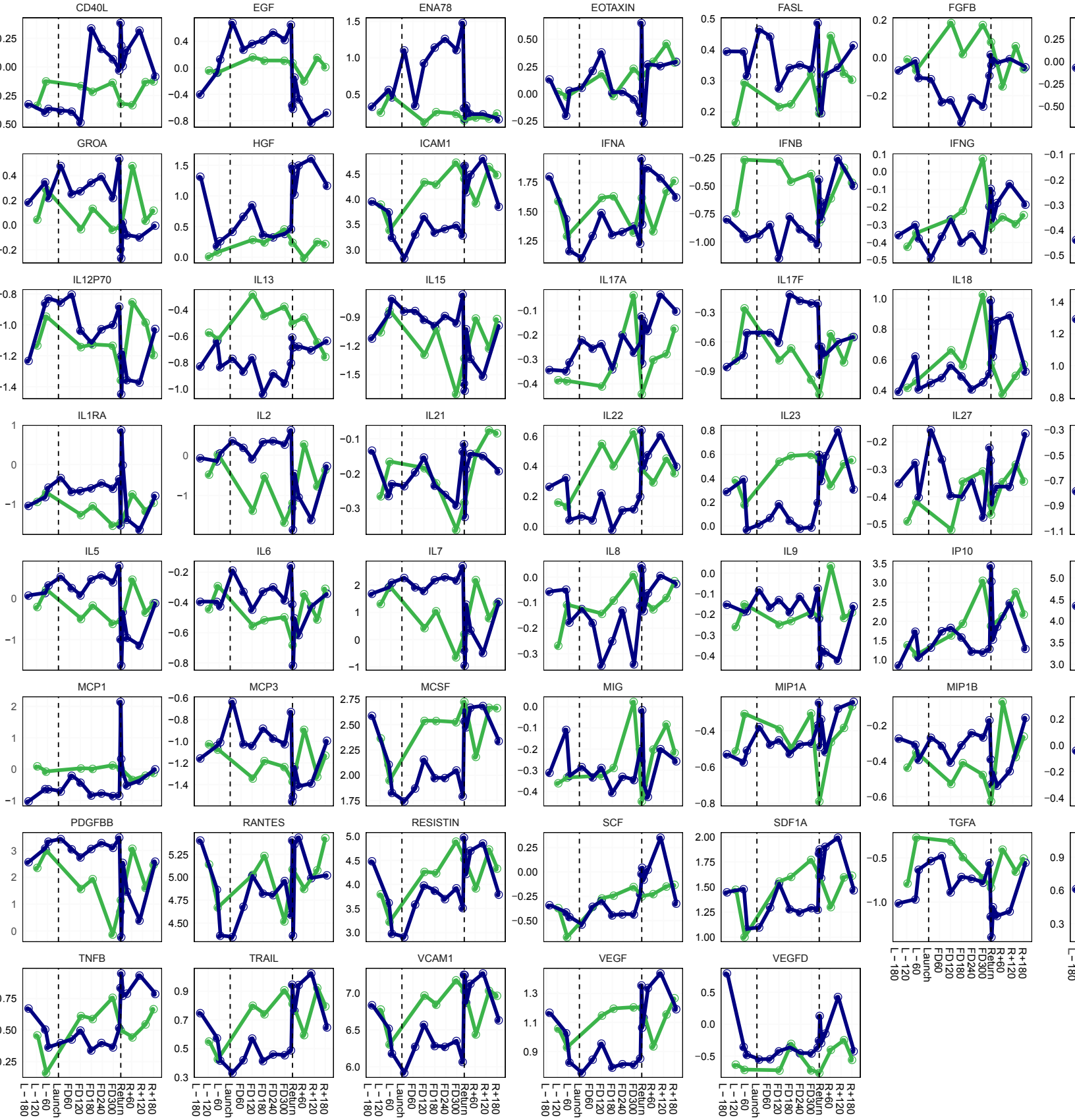

flight vs Pre+Post−flight change
cluding R+0, R+4
< 0.05

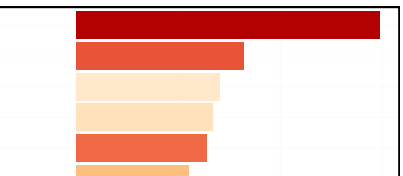

(F) In−flight vs Pre+Post-flight Change
Excluding R+0, R+4
q < 0.05

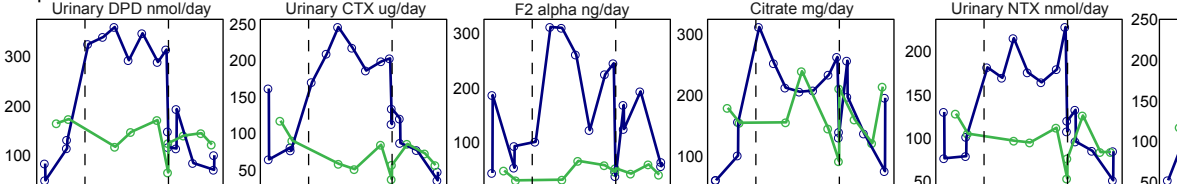

Fig. S8

Immune system responses to inflight and post-landing phase. (A,B) Cytokine profiles over time are plotted as percent difference from the mean of preflight value on the Y-axis, whereas X-axis is number of days during the mission. Two cytokines are representative of the highest spikes at the R+5 sample collection from TW: IL-1RA (in **A**) and CCL2 (in **B**). **(C)** CRP profile plotted as percent difference from the mean of preflight value on the Y-axis, whereas X-axis is number of days during the mission. (**D**) Profiles of all cytokines in each subject. Y-axis is normalized log-transformed (log2) fluorescence intensity, and X-axis is number of days during mission **(E)** Inflight vs pre- and postflight changes in biochemical markers and cytokines from blood and urine were ranked in terms of their degree of change and p-value. Colors are log10 of the q-value (<0.05, ANOVA). **(F)** Profiles of biochemical markers from blood and urine over time are plotted as percent difference from the mean of preflight value on the Y-axis, whereas X-axis is number of days during the mission. For all panels TW is blue and HR is green.

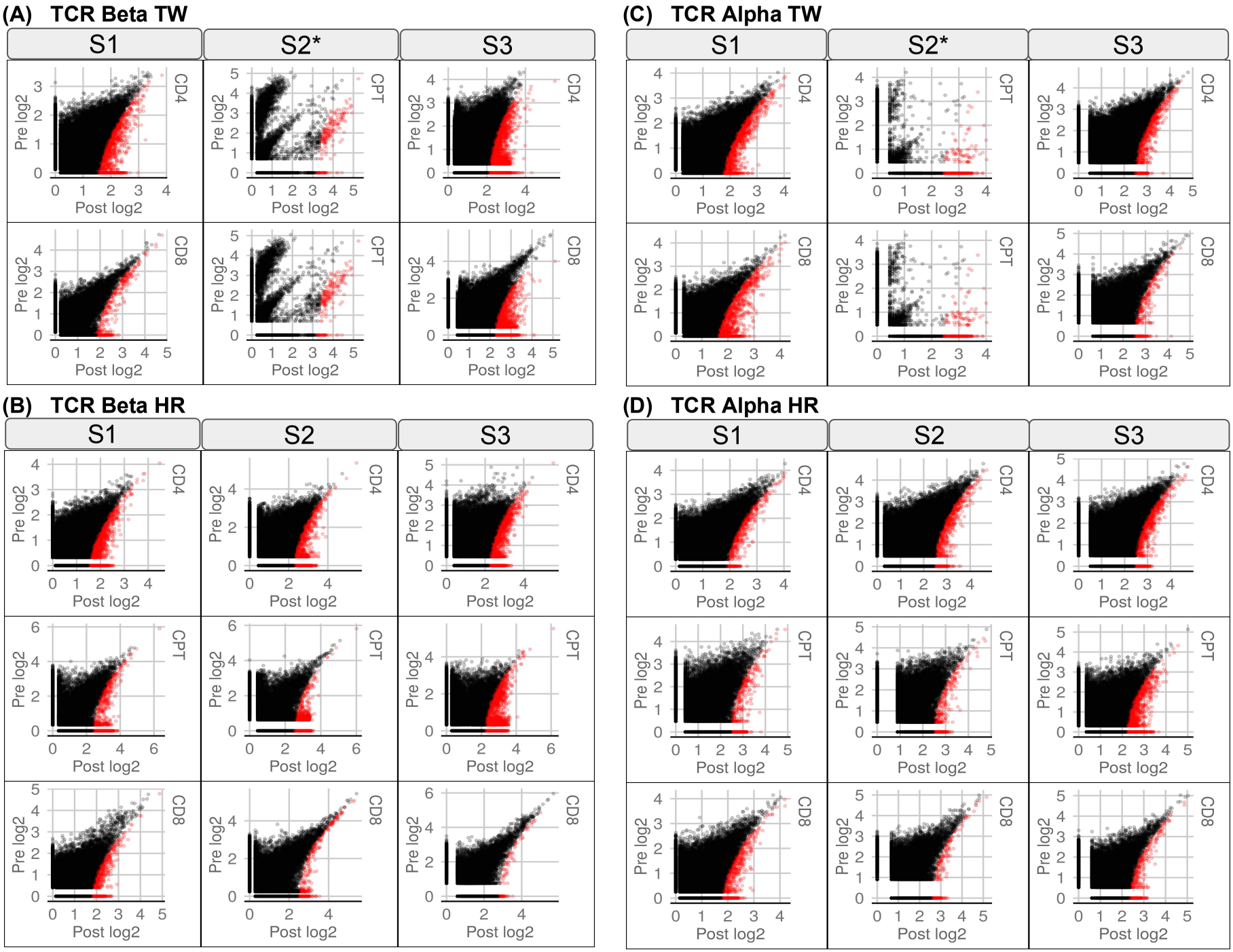
(A) TCR Beta TW
S1
S2*
S3
CD4
CPT
CD8
Pre log2
Post log2
(B) TCR Beta HR
S1
S2
S3
CD4
CPT
CD8
Pre log2
Post log2
(C) TCR Alpha TW
S1
S2*
S3
CD4
CPT
CD8
Pre log2
Post log2
(D) TCR Alpha HR
S1
S2
S3
CD4
CPT
CD8
Pre log2
Post log2

Fig. S9

Comparison of normalized clonal abundance pre-vs post-vaccination. The x-axis represents the post vaccination clonal abundance while the y-axis represents the clonal abundance at pre-vaccination. The shaded portion (red) represents the vaccination response (5% FDR adjusted) within each vaccination season and cell type for the same individual. **(A, C)** Clonotypes in the flight twin (TW) extracted from TCR Alphas and Betas respectively. The inflight time point is represented as S2*. **(B, D)** Clonal abundance in the ground-based twin (HR) who was also sampled across three vaccination seasons.

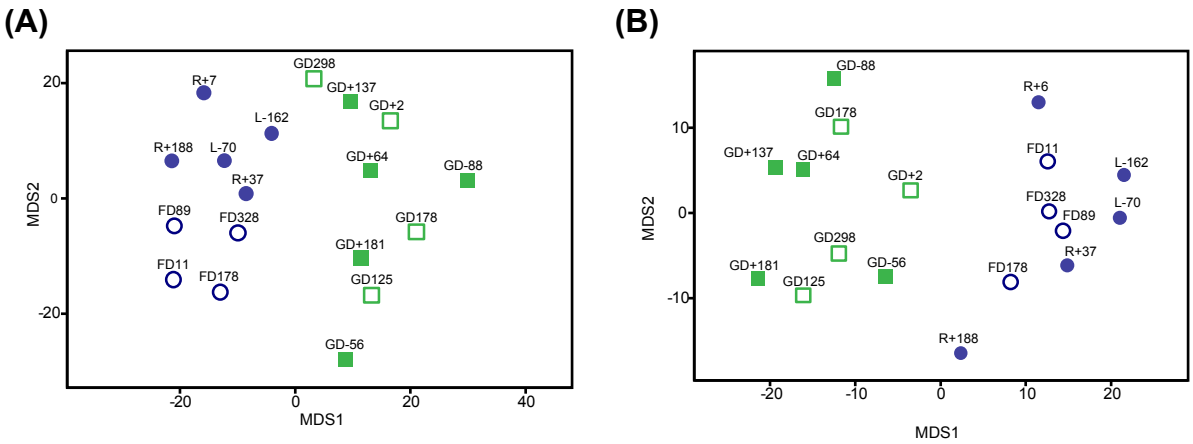
(A)
GD298
R+7
GD+137
GD+2
L-162
R+188
L-70
GD+64
GD-88
R+37
FD89
FD328
GD178
GD+181
FD11
FD178
GD125
GD-56
20
0
-20
MDS2
-20
0
20
40
MDS1
(B)
GD-88
R+6
GD178
GD+137
GD+64
FD11
L-162
GD+2
FD328
L-70
FD89
GD298
GD+181
GD-56
R+37
GD125
FD178
R+188
10
0
-10
MDS2
-20
-10
0
10
20
MDS1

Fig. S10

Viral and fungal representation in fecal microbiomes. (A) Metric multidimensional (mMDS) plot of fecal fungal microbial community from TW and HR. Samples are color coded by subject (TW=blue; HR=green), with open symbols representing flight samples from TW or flight-equivalent samples from HR. A strong separation of the two subjects across all time points was observed (analysis of similarity, ANOSIM, $R > 0.748$, $p<0.001$; taxonomic level of species). Fungi, represented 0.0051% to 0.0084% of annotated metagenome reads, consisted of 225 species-level taxa across both subjects. Within TW, the fungal communities identified inflight were significantly different from those pre- and postflight (ANOSIM $R=0.45$, $p<0.024$). Conversely, in HR, samples taken from the equivalent time points were not significantly different between inflight time period samplings compared to pre- and postflight samplings (ANOSIM, $R=-0.038$, $p=0.516$). 2D stress=0.26. **(B)** mMDS plot of fecal viral community composition from TW and HR. The viral community was comprised of 16 families, with most sequences deriving from viruses of the order Caudovirales and from the family Microviridae. Overall, most annotated viral sequences were derived from bacteriophages, and represented 0.0023% to 0.0121% of annotated metagenome reads. The two subjects had significantly different viromes (ANOSIM $R=0.916$, $p<0.001$). However, the viral community structures of the inflight versus pre-/postflight samples for both subjects were not significantly different (ANOSIM $R < -0.069$, $p>0.635$). 2D stress=0.12.

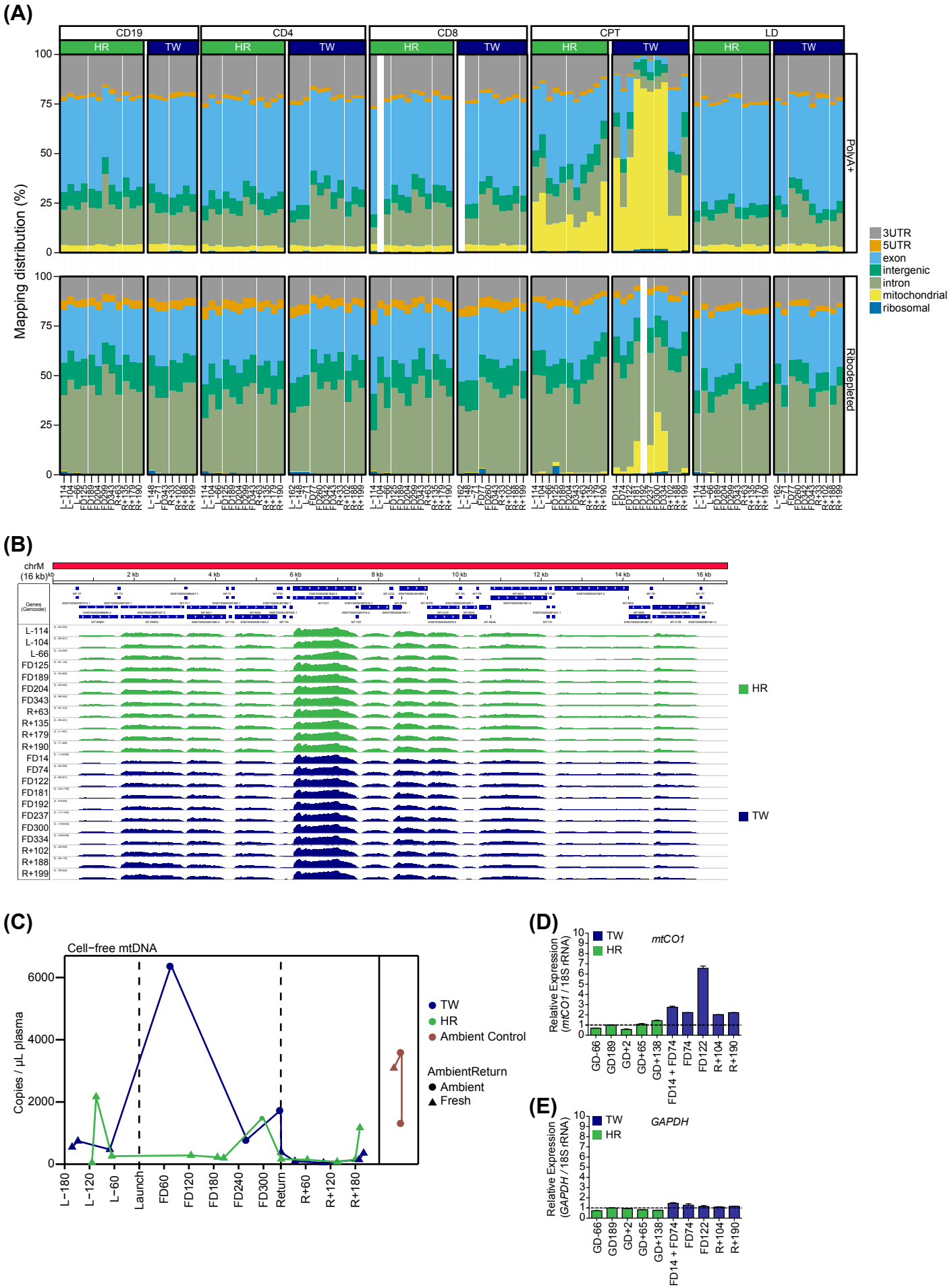
(A)
CD19
CD4
CD8
CPT
LD
HR
TW
Mapping distribution (%)
PolyA+
Ribodepleted
3UTR
5UTR
exon
intergenic
intron
mitochondrial
ribosomal
(B)
chrM
(16 kb)
Genes (Gencode)
HR
TW
(C)
Cell−free mtDNA
Copies / µL plasma
TW
HR
Ambient Control
AmbientReturn
Ambient
Fresh
L−180
L−120
L−60
Launch
FD60
FD120
FD180
FD240
FD300
Return
R+60
R+120
R+180
(D)
mtCO1
Relative Expression (mtCO1 / 18S rRNA)
GD-66
GD189
GD+2
GD+65
GD+138
FD14 + FD74
FD74
FD122
R+104
R+190
(E)
GAPDH
Relative Expression (GAPDH / 18S rRNA)

Fig. S11

Read distribution and validation for aligned reads in RNA-seq experiments. (A) Flight samples for TW show highly increased mitochondrial RNA in the last 6 months of the mission, as compared to HR. Colors represent reads mapped to the 3'UTR (grey), 5'UTR (orange), exon (light blue), intergenic (dark green), intron (sage), mitochondrial (yellow), and ribosomal regions (blue). This change is not seen in either HR or postflight samples of TW. **(B)** Flight days (left) and mapped read coverage across the mitochondrial genome (x-axis), as shown in the Integrated Genome Viewer (IGV) plot. Gene annotations (blue) are on top for mitochondrial genes. **(C)** Cell-free mitochondrial DNA analysis by qPCR. HR is green and TW is blue in all panels. **(D, E)** Mitochondrial RNA from CPT samples RT-PCR validation for TW, using primers for **(D)** *mtC01* on the mitochondrial genome, run in triplicate relative to 18S rRNA, which show a mid-flight increase in mtRNA that is not observed in **(E)** a control gene *GAPDH*.

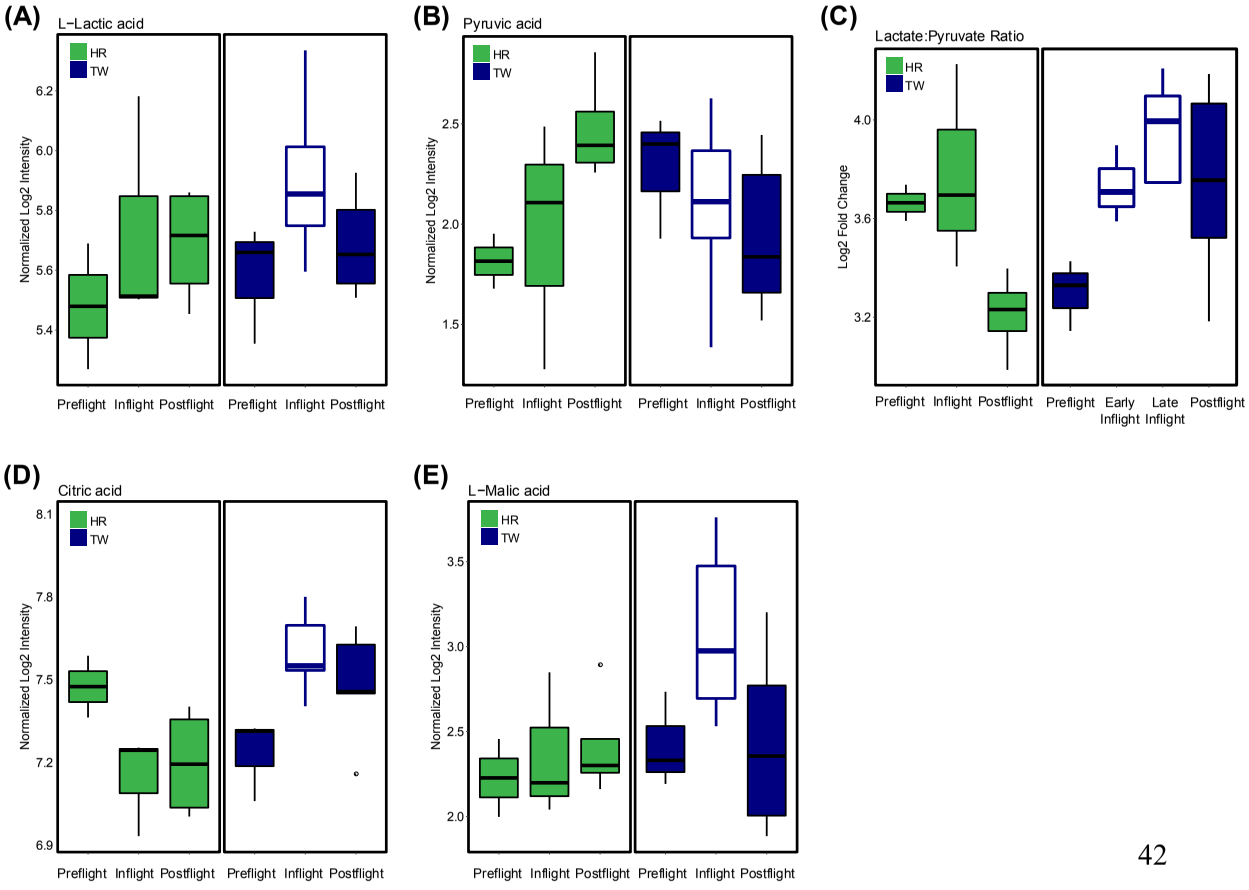
(A)
L−Lactic acid
HR
TW
Normalized Log2 Intensity
6.2
6.0
5.8
5.6
5.4
Preflight Inflight Postflight Preflight Inflight Postflight
(B)
Pyruvic acid
HR
TW
Normalized Log2 Intensity
2.5
2.0
1.5
Preflight Inflight Postflight Preflight Inflight Postflight
(C)
Lactate:Pyruvate Ratio
HR
TW
Log2 Fold Change
4.0
3.6
3.2
Preflight Inflight Postflight Preflight Early Inflight Late Inflight Postflight
(D)
Citric acid
HR
TW
Normalized Log2 Intensity
8.1
7.8
7.5
7.2
6.9
Preflight Inflight Postflight Preflight Inflight Postflight
(E)
L−Malic acid
HR
TW
Normalized Log2 Intensity
3.5
3.0
2.5
2.0
Preflight Inflight Postflight Preflight Inflight Postflight

Fig. S12

Plasma levels of metabolites related to mitochondrial respiration . Distributions of relative levels (log2 intensity) of **(A)** L-Lactic acid, **(B)** Pyruvic acid, **(C)** Lactic acid/Pyruvic acid ratio, **(D)** Citric acid, and **(E)** L-Malic acid from plasma during pre-, in- and postflight periods in HR and TW.

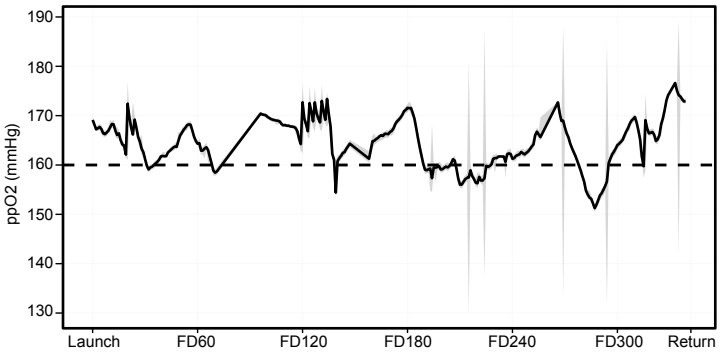
190
180
170
160
150
140
130
ppO2 (mmHg)
Launch
FD60
FD120
FD180
FD240
FD300
Return

Fig. S13

Oxygen levels on board ISS. Measurements of oxygen (ppO2; mmHg) recorded on the International Space Station over the duration of the mission.

(A) ACCURACY

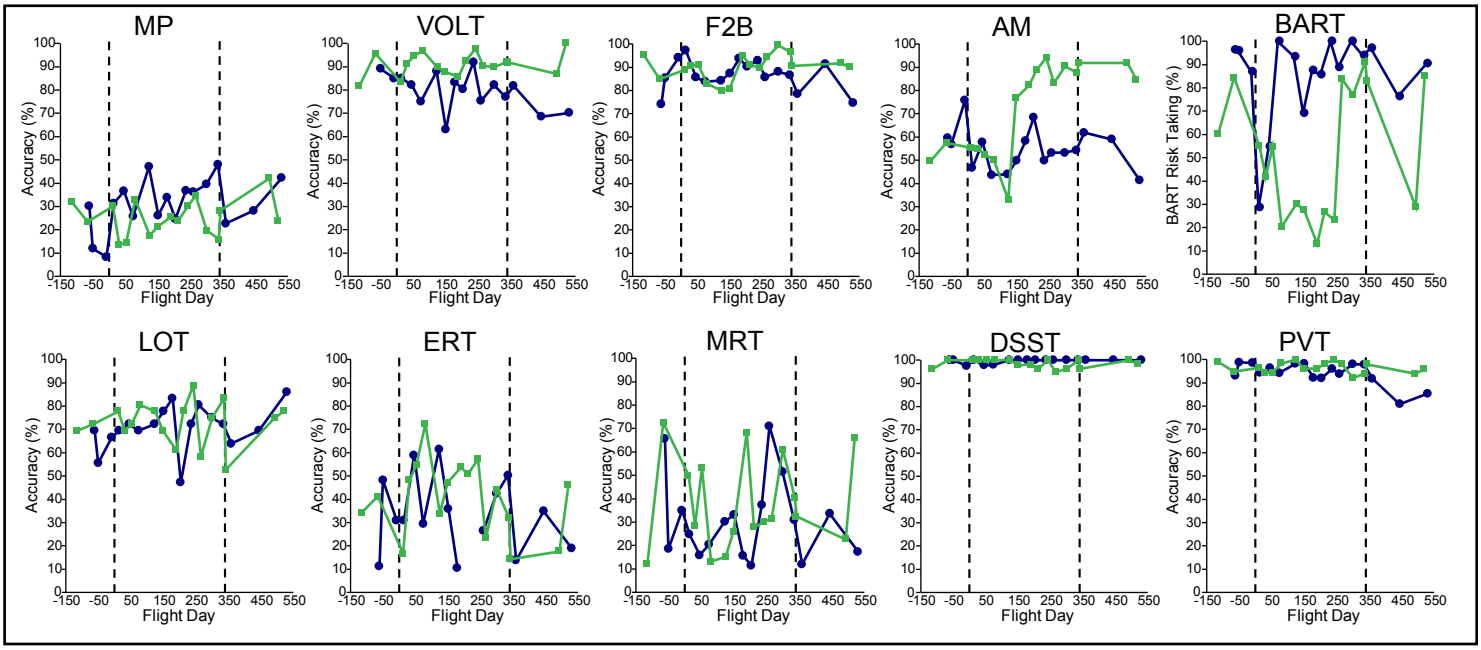

(B) SPEED

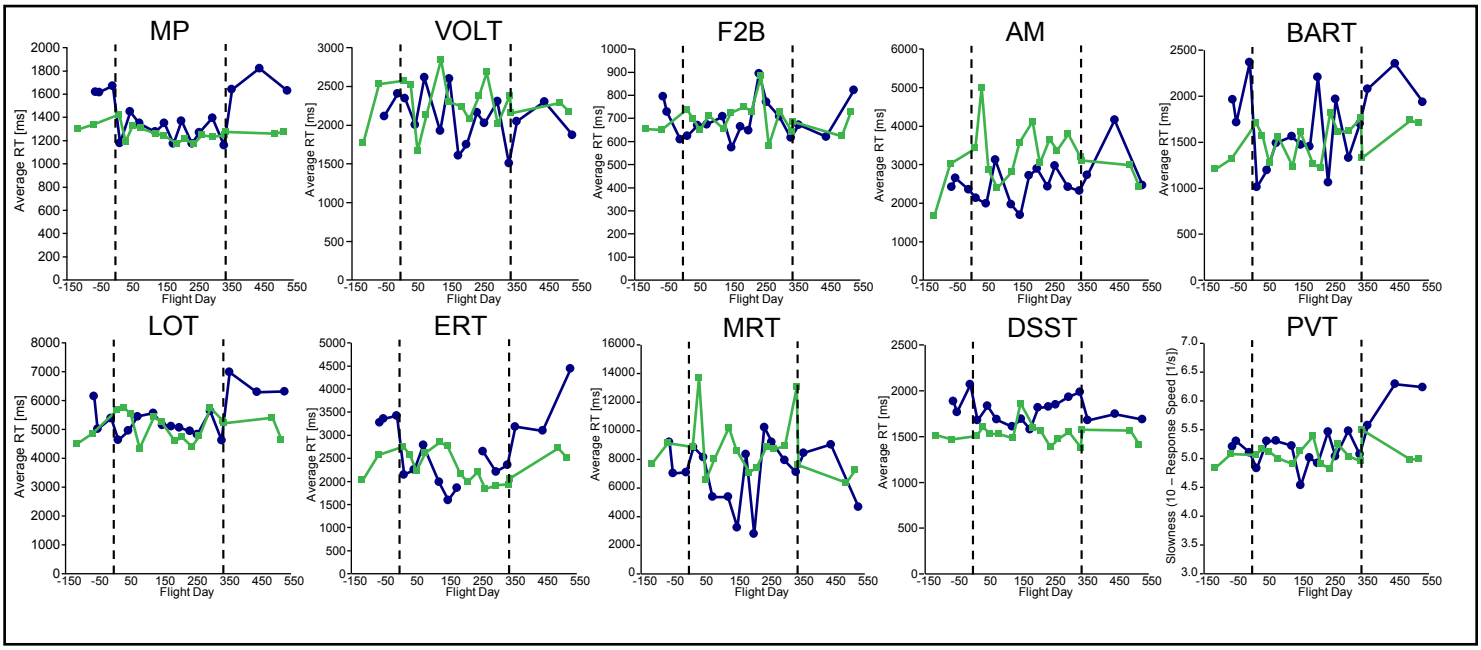

Fig. S14

Detailed comparison of TW versus HR for Cognitive Speed and Accuracy. Blue lines represent TW data and green lines represent HR data. The vertical lines indicate launch and landing dates for TW. For all tests, higher values represent **(A)** higher accuracy (in case of the BART, higher risk taking propensity) or **(B)** slower response speed. Average response time in milliseconds is shown for all speed tests except for the PVT. For the PVT, response times were reciprocally transformed and then subtracted from 10. MP: Motor Praxis; VOLT: Visual Object Learning; F2B: Fractal 2-Back; AM: Abstract Matching; LOT: Line Orientation; ERT: Emotion Recognition; MRT: Matrix Reasoning; DSST: Digit Symbol Substitution; BART: Balloon Analog Risk Test; PVT: Psychomotor Vigilance.

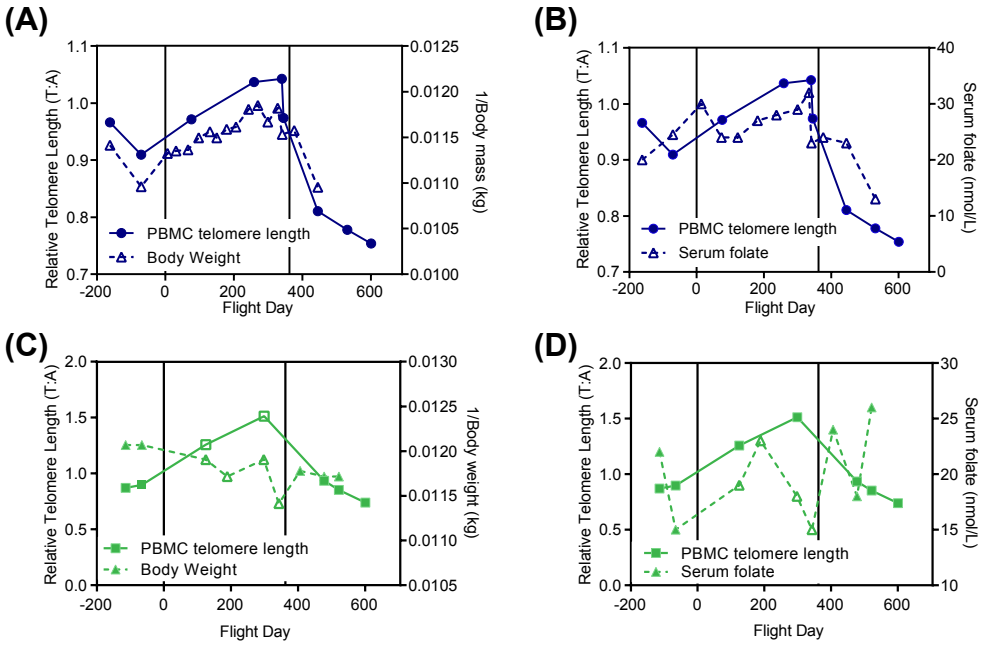
(A)
Relative Telomere Length (T:A)
1/Body mass (kg)
PBMC telomere length
Body Weight
Flight Day
(B)
Relative Telomere Length (T:A)
Serum folate (nmol/L)
PBMC telomere length
Serum folate
Flight Day
(C)
Relative Telomere Length (T:A)
1/Body weight (kg)
PBMC telomere length
Body Weight
Flight Day
(D)
Relative Telomere Length (T:A)
Serum folate (nmol/L)
PBMC telomere length
Serum folate
Flight Day

Fig. S15

Relationship between telomere length and folate levels. (A,B) Telomere length in TW (blue) plotted along with **(A)** body mass and **(B)** serum folate. **(C,D)** Same as in (A,B) for HR (green). PBMC telomere data are represented as circles; body mass and folate data are triangles.

Supplementary Tables

Table S1. Collection timepoints and analyses
Available online

Table S1

Collection time points and analyses table. Rows represent unique analyses performed. First 4 columns define the principal investigator (last name) supervising relevant analyses, subject (TW or HR), flight time (pre- ,in- ,or postflight), and NASA session (temporally related to launch (L), flight (FD) and return (R) time periods, as well as and ground subject (GD) for pre (-), in ( ), and post (+) flight). The next 2 columns define sample type and cell type (if blood derived). The last column defines the analysis performed. Cell type abbreviations: peripheral blood mononuclear cells (PBMCs), lymphocyte depleted cells (LD), CD4+, CD8+ or CD19+ enriched populations (CD4, CD8 or CD19 respectively). Analysis abbreviations: quantitative real-time polymerase chain reaction (qRT-PCR), T-cell receptor sequencing (TCR), telomere fluorescence in situ hybridization (Telo-FISH), whole-genome bisulfite sequencing (WGBS), RNA-sequencing (RNA-seq).

Table S2. Differential gene expression gene set analysis results
Available online

Table S2

Differential gene expression gene set analysis results. Different worksheets show (1) the overall summary statistics, (2,3) details of differentially expressed genes for different comparisons at different q-values (0.05 and 0.01, DESeq2 multivariate negative binomial model) and cell types, (4) detailed information on all differentially expressed genes, and (5) significantly altered pathways from Gene Set Enrichment Analysis (GSEA).

Table S3. Summary of differential testing for untargeted and targeted metabolomics data
Available online

Table S3

Summary of differential testing for untargeted and targeted metabolomics data. The first sheet has an overview of the linear models fit to the untargeted plasma metabolomics data, including the coefficients and contrasts tested. The second sheet lists metabolites identified in Sheet 1 as significantly differential (adjusted p-value < 0.05) in any comparison, as well as adjusted p-values for each coefficient or contrast of interest. The third sheet lists targeted metabolites identified in urine and plasma samples.

Table S4. Gene ontology results based on the Jensen-Shannon distance of DNA methylation within promoters.
Available online

Table S4

Gene ontology results based on the Jensen-Shannon distance of DNA methylation within promoters. Different worksheets display the gene ontology results obtained using the indicated gene ranking list from Table S4 associated with each comparison. For example, worksheet 1 (CD4_HR_Pre_vs_Inflight1) represents the results from comparing preflight to the first inflight time point in CD4 cells from HR, whereas the worksheet named "CD4_TW_vs_HR_PostFlight" contains results from comparison of CD4 cells collected postflight between TW and HR. "Inflight1" and "Inflight2" represent the first and second in-flight time points, respectively, while "RankProd_Inflight" represents the rank product of both in-flight time points. (Terms: P.value = uncorrected enrichment p-value computed according to hypergeometric test; FDR.q.value = Benjamini-Hochberg corrected p.value; Enrichment = (b/n) / (B/N); N = total number of genes; B = total number of genes associated with GO term;n = number of genes in the top of user's input list; b = number of genes in the intersection.)

Table S5. Gene rankings based on the Jensen-Shannon distance of DNA methylation within promoters.
Available online

Table S5

Gene rankings based on the Jensen-Shannon distance of DNA methylation within promoters. Different worksheets contain gene rankings from comparisons (1) within HR, (2) within TW, and (3) between TW and HR. “Inflight1” and “Inflight2” represent the first and second in-flight time points, respectively, while “RankProd_Inflight” represents the rank product of both in-flight time points.

Table S6. Summary of differential testing for cytokine data.
Available online

Table S6

Summary of differential testing for cytokine data. The first sheet has an overview of the linear models fit to the data, including the coefficients and contrasts tested. The second sheet lists cytokines identified as significantly differential (adjusted p-value < 0.05) in any comparison, as well as adjusted p-values for each coefficient or contrast of interest. The third sheet lists results of functional term enrichments from the web-based tool DAVID, using the Functional Annotation Chart.

Table S7. Cardiovascular and Ocular Parameters.
Complete data set from the flight (TW) and ground (HR) twin collected using ultrasound, optical coherence tomography and automated blood pressure cuff.

		Flight Twin							Ground Twin				
		L-53		FD62	FD157	FD285	R+12		GD-114		GD189	GD+2	
	Units	Seated	Supine	Flight	Flight	Flight	Seated	Supine	Seated	Supine	Flight	Seated	Supine
Forehead Tissue Thickness	cm	0.60	0.69	0.78	0.72	0.78	0.61	0.66	ND	0.59	0.59	0.59	0.59
Internal Jugular Vein Area	mm^2	12.3	74.2	67.1	66.8	62.3	4.0	59.0	11.8	93.2	116.9	9.1	80.6
Choroid Thickness	µm	351	319	ND	367	360	359	333	336	338	320	320	330
Total Retinal Thickness	µm	424	420	537	542	509	471	469	451	439	442	449	447
Systolic Blood Pressure	mmHg	143	128	126	122	125	136	126	122	112	113	125	118
Diastolic Blood Pressure	mmHg	89	79	76	69	76	79	68	78	75	63	85	72
Mean Arterial Pressure	mmHg	107	95	93	87	93	98	87	92	87	80	98	87
Pulse Pressure	mmHg	54	49	50	53	49	57	58	44	37	50	40	46
Cardiac Output	L/min	4.80	6.96	6.00	5.98	5.78	3.89	6.48	4.25	ND	5.59	3.66	4.50
Stroke Volume	mL/beat	76.6	110.9	94.7	95.4	84.1	60.5	100.7	76.1	ND	97.3	59.5	73.1
Heart Rate	beats/min	62	62	63	63	64	64	63	61	53	54	61	59
Systemic Vascular Resistance	mmHg/L/min	22.3	13.6	15.5	14.5	16.0	25.2	13.4	21.7	ND	14.2	26.7	19.4
Mitral E Wave	cm/s	53	83	65	81	67	50	98	562	ND	638	514	801
Mitral A Wave	cm/s	58	61	50	49	47	48	73	517	ND	548	499	628
MitralE/A Ratio		0.92	1.38	1.31	1.65	1.42	1.04	1.34	1.09	ND	1.17	1.03	1.28

		Flight Twin									Ground Twin		
		L-163	L-72	Average	FD13	FD74	FD181	FD238	FD299	FD332	R+4	GD-66	GD190	GD+2
Carotid Intima-Media Thickness	mm	0.509	0.600	0.555	0.702	0.680	0.691	0.695	0.710	0.696	0.677	0.575	0.643	0.563
Carotid Systolic Diameter	mm	6.9	6.8	6.9	7.4	7.2	7.2	7.2	7.5	7.5	7.1	7.0	7.1	7.1
Carotid Diastoloc Diameter	mm	6.6	6.6	6.6	7.1	6.9	6.8	6.8	7.2	7.2	6.8	6.6	6.8	6.8

		Flight Twin															Ground Twin				
		L-163		L-72		Average		FD13	FD74	FD181	FD238	FD299	FD332	AVG	R+4		GD-66		GD190	GD+2	
	Units	Seated	Supine	Seated	Supine	Seated	Supine	Flight	Flight	Flight	Flight	Flight	Flight	Flight	Seated	Supine	Seated	Supine	Flight	Seated	Supine
Heart Rate	beats/min	67	63	73	70	70	67	65	63	60	69	62	60	63	69	74	62	60	59	65	66
Systolic Blood Pressure	mmHg	143	133	155	132	149	133	120	ND	120	121	129	128	124	129	122	128	113	126	137	136
Diastolic Blood Pressure	mmHg	85	78	90	78	88	78	64	ND	79	79	72	75	74	70	63	80	61	72	74	72
Mean Arterial Pressure	mmHg	104	96	112	96	108	96	83	ND	93	93	91	93	90	90	83	96	78	90	95	93
Pulse Pressure	mmHg	58	55	65	54	62	55	56	ND	41	42	57	53	50	59	59	48	52	54	63	64
Cardiac Output	L/min	5.15	6.32	4.99	6.49	5.07	6.41	4.88	6.21	4.53	6.84	4.80	6.61	5.65	5.75	7.45	4.88	5.39	5.49	4.70	4.85
Stroke Volume	mL/beat	78	99	68	94	73	96	80	98	77	103	74	91	87	79	100	78	89	92	69	77
Systemic Vascular Resistance	mmHg/L/min	20.3	15.2	22.4	14.8	21.3	15.0	16.9	ND	20.5	13.6	19.0	14.0	17	15.6	11.1	19.7	14.5	19.1	21.9	20.8

Table S7

Cardiovascular and Ocular Parameters. Complete data set from the flight (TW) and ground (HR) subjects collected using ultrasound, optical coherence tomography and automated blood pressure cuff.

Table S8. Biochemical profile data
Available online

Table S8

Biochemical profile data. Targeted markers of physiological and nutritional status, including general chemistry, minerals, vitamins, cytokines, etc. Data are presented for the flight subject (TW) from sample collections preflight (Launch minus, L-162 and L-71 days); inflight (Flight Day, FD, FD14, FD74/122 averaged, FD181, and FD237), and postflight, (Return plus, R+, 0 days, R+4, R+35, R+104, and R+190 days). Data for the ground subject (HR; blood n=9; urine n=10) were averaged and show in the table as mean ± SD. Urine data represent the average of two 24-h urine collections. An extra sample was collected at L-71 and processed like the inflight samples, i.e., these were collected, centrifuged, and frozen in the tube with thawing and analysis postflight.

Table S9. Summary of RNA-sequencing quality control metrics.
Available online

Table S9

Summary of RNA-sequencing quality control metrics. RNA Integrity numbers (RIN), total number of sequencing reads, GC content, duplication rate, alignment rate and rate of assignment to elements in the reference annotation are given for both PolyA+ and rRNA depleted experiments for all samples.

Table S10. Summary of shotgun metagenome sequence annotation.

Paired-end sequences were annotated for taxonomy and gene function using the software packages DIAMOND, MEGAN, and SUPER-FOCUS.

# Sample	Sample Date	Raw reads (both ends)	Phylum total counts	Phylum %	Class total counts	Class %	Order total counts	Order %	Family total counts	Family %	Genus total counts	Genus %	Species total counts	Species %	Functional (SEED) total counts	Functional (SEED) %
MHV-HR1	GD-88	31,330,500	12,501,912	39.9	11,952,064	38.1	11,928,842	38.1	10,163,116	32.4	8,681,815	27.7	6,378,103	20.4	10,491,423	33.5
MHV-HR2	GD-56	31,422,178	12,262,310	39	11,308,352	36	11,282,317	35.9	9,465,573	30.1	7,792,083	24.8	6,481,595	20.6	11,647,879	37.1
MHV-HR3	GD125	31,443,670	12,953,633	41.2	12,566,785	40	12,546,000	39.9	11,120,550	35.4	9,872,930	31.4	6,438,833	20.5	14,177,227	45.1
MHV-HR4	GD178	32,430,048	13,425,116	41.4	13,069,622	40.3	13,050,253	40.2	11,671,654	36	10,526,329	32.5	6,578,223	20.3	13,274,634	40.9
MHV-HR5	GD298	31,077,828	13,589,904	43.7	13,320,067	42.9	13,308,289	42.8	12,250,939	39.4	11,340,309	36.5	6,009,399	19.3	15,284,434	49.2
MHV-HR6	GD+2	30,219,338	12,659,727	41.9	12,201,878	40.4	12,184,467	40.3	10,672,699	35.3	9,459,939	31.3	6,113,865	20.2	12,475,552	41.3
MHV-HR7	GD+64	30,387,498	12,916,154	42.5	12,546,114	41.3	12,531,677	41.2	11,317,780	37.2	10,279,139	33.8	6,371,291	21	13,264,644	43.7
MHV-HR8	GD+137	29,839,526	12,699,620	42.6	12,324,070	41.3	12,313,216	41.3	11,318,707	37.9	10,535,489	35.3	5,863,823	19.7	14,451,129	48.4
MHV-HR9	GD+181	31,808,294	13,449,180	42.3	13,103,503	41.2	13,087,005	41.1	11,936,263	37.5	10,929,814	34.4	6,511,012	20.5	15,676,861	49.3
MHV-TW1	L-162	30,534,522	13,437,423	44	13,179,309	43.2	13,168,499	43.1	12,023,974	39.4	10,879,549	35.6	6,007,599	19.7	16,397,268	53.7
MHV-TW2	L-70	31,230,210	13,450,740	43.1	13,162,725	42.1	13,148,896	42.1	11,761,859	37.7	10,313,358	33	6,981,087	22.4	14,300,517	45.8
MHV-TW3	FD11	31,205,558	13,128,868	42.1	12,892,030	41.3	12,874,452	41.3	11,201,877	35.9	9,507,917	30.5	6,911,942	22.1	12,504,278	40.1
MHV-TW4	FD328	30,366,356	12,944,219	42.6	12,601,496	41.5	12,586,286	41.4	11,155,239	36.7	9,701,909	31.9	6,862,926	22.6	13,026,484	42.9
MHV-TW5	FD89	30,015,168	12,725,700	42.4	12,483,066	41.6	12,468,620	41.5	10,897,850	36.3	9,239,627	30.8	6,516,965	21.7	12,235,403	40.8
MHV-TW6	FD178	31,376,062	13,015,327	41.5	12,719,808	40.5	12,699,033	40.5	10,789,602	34.4	9,142,186	29.1	7,062,510	22.5	11,799,606	37.6
MHV-TW7	R+6	30,266,736	13,025,352	43	12,832,336	42.4	12,819,028	42.4	11,119,013	36.7	8,775,702	29	6,313,328	20.9	12,366,058	40.9
MHV-TW8	R+37	30,456,326	13,139,679	43.1	12,940,262	42.5	12,927,213	42.4	11,528,305	37.9	10,200,408	33.5	6,309,552	20.7	13,885,084	45.6
MHV-TW9	R+188	29,707,594	12,915,168	43.5	12,666,541	42.6	12,653,134	42.6	11,481,149	38.6	10,229,089	34.4	6,317,078	21.3	14,674,771	49.4

Table S10

Summary of shotgun metagenome sequence annotation. Paired-end sequences were annotated for taxonomy and gene function using the software packages DIAMOND, MEGAN, and SUPER-FOCUS. Total numbers of sequences are shown, followed by number and percentage of reads annotated to the taxonomic level of phylum to species. Total number and percentage of reads annotated at the SEED functional level are also shown.

Table S11. Summary of whole-genome bisulfite-sequencing data.
Alignment information, bisulfite conversion rate, CpG coverage and depth information are reported for each sample.

Sample	Number sequenced PE reads	Number aligned PE reads	Alignment rate (%)	Bisulfite conversion rate (%)	Number covered CpGs	Covered CpGs (%)	Mean depth
FD76_TW_AR_CD4	247985848	193779492	78	99.65	27606014	98	13.30640211
FD76_TW_AR_CD8	277397578	216098797	78	99.63	26343079	93	14.75521828
GD125_HR_FR_CD4	229194971	185679511	81	99.66	27602469	98	12.94177852
GD125_HR_FR_CD8	334061977	252053849	75	99.66	26282210	93	14.42483542
FD259_TW_AR_CD4	237237014	187504431	79	99.69	27579691	98	12.81039904
FD259_TW_AR_CD8	328081015	247990617	76	99.67	26332130	93	15.12486132
GD298_HR_FR_CD4	258105402	210749862	82	99.65	27605411	98	14.18129352
GD298_HR_FR_CD8	319688354	246283657	77	99.66	26323900	93	14.98637985
R+104_TW_FR_CD4	303868717	248202660	82	99.68	27638634	98	17.21055541
R+104_TW_FR_CD8	282329966	219060701	78	99.67	26339375	93	14.34730914
GD+137_HR_FR_CD4	245162511	197559649	81	99.69	27580234	98	26.34427596
GD+137_HR_FR_CD8	347788362	268049123	77	99.67	26326753	93	16.13913413
L-162_TW_FR_CD4	341320987	257980373	76	99.73	27603964	98	26.82118771
L-162_TW_FR_CD8	281787040	214075985	76	99.71	27505003	97	13.00117018
GD-114_HR_FR_CD4	348087146	270723762	78	99.7	27626869	98	29.48471608
GD-114_HR_FR_CD8	277597706	212763699	77	99.73	27522793	98	13.03383342

Table S11

Summary of whole-genome bisulfite-sequencing data. Alignment information, bisulfite conversion rate, CpG coverage and depth information are reported for each sample.

References and Notes

1. M. Barratt, S. L. Pool, Eds., *Principles of Clinical Medicine for Space Flight* (Springer, 2008).

2. V. A. Convertino, "Exercise and adaptation to microgravity environments" in *Supplement 14: Handbook of Physiology*, *Environmental Physiology*, *Comprehensive Physiology* (Wiley, 2011), pp. 815–843.

3. W. E. Thornton, T. P. Moore, S. L. Pool, Fluid shifts in weightlessness. *Aviat. Space Environ. Med.* **58**, A86–A90 (1987). Medline

4. C. S. Leach, C. P. Alfrey, W. N. Suki, J. I. Leonard, P. C. Rambaut, L. D. Inners, S. M. Smith, H. W. Lane, J. M. Krauhs, Regulation of body fluid compartments during short-term spaceflight. *J. Appl. Physiol.* **81**, 105–116 (1996). doi:10.1152/jappl.1996.81.1.105 Medline

5. J. V. Meck, C. J. Reyes, S. A. Perez, A. L. Goldberger, M. G. Ziegler, Marked exacerbation of orthostatic intolerance after long- vs. short-duration spaceflight in veteran astronauts. *Psychosom. Med.* **63**, 865–873 (2001). doi:10.1097/00006842-200111000-00003 Medline

6. S. M. C. Lee, A. H. Feiveson, S. Stein, M. B. Stenger, S. H. Platts, Orthostatic intolerance after ISS and Space Shuttle missions. *Aerosp. Med. Hum. Perform.* **86** (suppl. 1), A54–A67 (2015). doi:10.3357/AMHP.EC08.2015 Medline

7. T. P. Moore, W. E. Thornton, Space shuttle inflight and postflight fluid shifts measured by leg volume changes. *Aviat. Space Environ. Med.* **58**, A91–A96 (1987). Medline

8. M. A. Perhonen, F. Franco, L. D. Lane, J. C. Buckey, C. G. Blomqvist, J. E. Zerwekh, R. M. Peshock, P. T. Weatherall, B. D. Levine, Cardiac atrophy after bed rest and spaceflight. *J. Appl. Physiol.* **91**, 645–653 (2001). doi:10.1152/jappl.2001.91.2.645 Medline

9. H. Akima, Y. Kawakami, K. Kubo, C. Sekiguchi, H. Ohshima, A. Miyamoto, T. Fukunaga, Effect of short-duration spaceflight on thigh and leg muscle volume. *Med. Sci. Sports Exerc.* **32**, 1743–1747 (2000). doi:10.1097/00005768-200010000-00013 Medline

10. R. Gopalakrishnan, K. O. Genc, A. J. Rice, S. M. C. Lee, H. J. Evans, C. C. Maender, H. Ilaslan, P. R. Cavanagh, Muscle volume, strength, endurance, and exercise loads during 6-month missions in space. *Aviat. Space Environ. Med.* **81**, 91–104 (2010). doi:10.3357/ASEM.2583.2010 Medline

11. S. Trappe, D. Costill, P. Gallagher, A. Creer, J. R. Peters, H. Evans, D. A. Riley, R. H. Fitts, Exercise in space: Human skeletal muscle after 6 months aboard the International Space Station. *J. Appl. Physiol.* **106**, 1159–1168 (2009). doi:10.1152/japplphysiol.91578.2008 Medline

12. J. C. Hayes, M. E. Guilliams, S. M. C. Lee, K. R. MacNeill, A. D. M. Jr, "Exercise: developing countermeasure systems for optimizing astronaut performance in space" in *Biomedical Results of the Space Shuttle Program*, D. Risin, P. C. Stepaniak, Eds. (NASA/SP-2013-607, NASA, Washington, DC, 2013), pp. 289–314.

13. S. M. Smith, M. A. Heer, L. C. Shackelford, J. D. Sibonga, L. Ploutz-Snyder, S. R. Zwart, Benefits for bone from resistance exercise and nutrition in long-duration spaceflight: Evidence from biochemistry and densitometry. *J. Bone Miner. Res.* **27**, 1896–1906 (2012). doi:10.1002/jbmr.1647 Medline

14. T. H. Mader, C. R. Gibson, A. F. Pass, L. A. Kramer, A. G. Lee, J. Fogarty, W. J. Tarver, J. P. Dervay, D. R. Hamilton, A. Sargsyan, J. L. Phillips, D. Tran, W. Lipsky, J. Choi, C. Stern, R. Kuyumjian, J. D. Polk, Optic disc edema, globe flattening, choroidal folds, and hyperopic shifts

observed in astronauts after long-duration space flight. *Ophthalmology* **118**, 2058–2069 (2011). doi:10.1016/j.ophtha.2011.06.021 Medline

15. L. F. Zhang, A. R. Hargens, Spaceflight-induced intracranial hypertension and visual impairment: Pathophysiology and countermeasures. *Physiol. Rev.* **98**, 59–87 (2018). doi:10.1152/physrev.00017.2016 Medline

16. M. B. Stenger *et al*., "Evidence report: Risk of spaceflight associated neuro-ocular syndrome (SANS)" (NASA, Lyndon B. Johnson Space Center, Houston, 2018).

17. M. V. Carminati, D. Griffith, M. R. Campbell, Sub-orbital commercial human spaceflight and informed consent. *Aviat. Space Environ. Med.* **82**, 144–146 (2011). doi:10.3357/ASEM.2846.2011 Medline

18. K. Contrepois, L. Jiang, M. Snyder, Optimized analytical procedures for the untargeted metabolomic profiling of human urine and plasma by combining hydrophilic interaction (HILIC) and reverse-phase liquid chromatography (RPLC)-mass spectrometry. *Mol. Cell. Proteomics* **14**, 1684–1695 (2015). doi:10.1074/mcp.M114.046508 Medline

19. E. C. Borresen, D. G. Brown, G. Harbison, L. Taylor, A. Fairbanks, J. O'Malia, M. Bazan, S. Rao, S. M. Bailey, M. Wdowik, T. L. Weir, R. J. Brown, E. P. Ryan, A randomized controlled trial to increase navy bean or rice bran consumption in colorectal cancer survivors. *Nutr. Cancer* **68**, 1269–1280 (2016). doi:10.1080/01635581.2016.1224370 Medline

20. R. M. Cawthon, Telomere length measurement by a novel monochrome multiplex quantitative PCR method. *Nucleic Acids Res.* **37**, e21 (2009). doi:10.1093/nar/gkn1027 Medline

21. L. S. Honig, M. S. Kang, R. Cheng, J. H. Eckfeldt, B. Thyagarajan, C. Leiendecker-Foster, M. A. Province, J. L. Sanders, T. Perls, K. Christensen, J. H. Lee, R. Mayeux, N. Schupf, Heritability of telomere length in a study of long-lived families. *Neurobiol. Aging* **36**, 2785–2790 (2015). doi:10.1016/j.neurobiolaging.2015.06.017 Medline

22. J. Lin, J. Cheon, R. Brown, M. Coccia, E. Puterman, K. Aschbacher, E. Sinclair, E. Epel, E. H. Blackburn, Systematic and cell type-specific telomere length changes in subsets of lymphocytes. *J. Immunol. Res.* **2016**, 5371050 (2016). doi:10.1155/2016/5371050 Medline

23. P. M. Lansdorp, N. P. Verwoerd, F. M. van de Rijke, V. Dragowska, M. T. Little, R. W. Dirks, A. K. Raap, H. J. Tanke, Heterogeneity in telomere length of human chromosomes. *Hum. Mol. Genet.* **5**, 685–691 (1996). doi:10.1093/hmg/5.5.685 Medline

24. B. J. Sishc, C. B. Nelson, M. J. McKenna, C. L. R. Battaglia, A. Herndon, R. Idate, H. L. Liber, S. M. Bailey, Telomeres and telomerase in the radiation response: Implications for instability, reprograming, and carcinogenesis. *Front. Oncol.* **5**, 257 (2015). doi:10.3389/fonc.2015.00257 Medline

25. C. W. Greider, E. H. Blackburn, Identification of a specific telomere terminal transferase activity in Tetrahymena extracts. *Cell* **43**, 405–413 (1985). doi:10.1016/0092-8674(85)90170-9 Medline

26. M. Hou, D. Xu, M. Björkholm, A. Gruber, Real-time quantitative telomeric repeat amplification protocol assay for the detection of telomerase activity. *Clin. Chem.* **47**, 519–524 (2001). Medline

27. F. A. Cucinotta, Space radiation risks for astronauts on multiple International Space Station missions. *PLOS ONE* **9**, e96099 (2014). doi:10.1371/journal.pone.0096099 Medline

28. K. George, J. Rhone, A. Beitman, F. A. Cucinotta, Cytogenetic damage in the blood lymphocytes of astronauts: Effects of repeat long-duration space missions. *Mutat. Res.* **756**, 165–169 (2013). doi:10.1016/j.mrgentox.2013.04.007 Medline

29. F. A. Ray, E. Zimmerman, B. Robinson, M. N. Cornforth, J. S. Bedford, E. H. Goodwin, S. M. Bailey, Directional genomic hybridization for chromosomal inversion discovery and detection. *Chromosome Res.* **21**, 165–174 (2013). doi:10.1007/s10577-013-9345-0 Medline

30. F. A. Ray, E. Robinson, M. McKenna, M. Hada, K. George, F. Cucinotta, E. H. Goodwin, J. S. Bedford, S. M. Bailey, M. N. Cornforth, Directional genomic hybridization: Inversions as a potential biodosimeter for retrospective radiation exposure. *Radiat. Environ. Biophys.* **53**, 255–263 (2014). doi:10.1007/s00411-014-0513-1 Medline

31. M. N. Cornforth, M. Durante, Radiation quality and intra-chromosomal aberrations: Size matters. *Mutat. Res.* **836** (part A), 28–35 (2018). doi:10.1016/j.mrgentox.2018.05.002 Medline

32. K. George, L. J. Chappell, F. A. Cucinotta, Persistence of space radiation induced cytogenetic damage in the blood lymphocytes of astronauts. *Mutat. Res.* **701**, 75–79 (2010). doi:10.1016/j.mrgentox.2010.02.007 Medline

33. G. Jenkinson, E. Pujadas, J. Goutsias, A. P. Feinberg, Potential energy landscapes identify the information-theoretic nature of the epigenome. *Nat. Genet.* **49**, 719–729 (2017). doi:10.1038/ng.3811 Medline

34. A. Koyanagi, C. Sekine, H. Yagita, Expression of Notch receptors and ligands on immature and mature T cells. *Biochem. Biophys. Res. Commun.* **418**, 799–805 (2012). doi:10.1016/j.bbrc.2012.01.106 Medline

35. M. Nakaya, Y. Xiao, X. Zhou, J.-H. Chang, M. Chang, X. Cheng, M. Blonska, X. Lin, S.-C. Sun, Inflammatory T cell responses rely on amino acid transporter ASCT2 facilitation of glutamine uptake and mTORC1 kinase activation. *Immunity* **40**, 692–705 (2014). doi:10.1016/j.immuni.2014.04.007 Medline

36. J. E. Thaventhiran, D. T. Fearon, L. Gattinoni, Transcriptional regulation of effector and memory $CD8^+$ T cell fates. *Curr. Opin. Immunol.* **25**, 321–328 (2013). doi:10.1016/j.coi.2013.05.010 Medline

37. J. de Batlle, J. Sauleda, E. Balcells, F. P. Gómez, M. Méndez, E. Rodriguez, E. Barreiro, J. J. Ferrer, I. Romieu, J. Gea, J. M. Antó, J. Garcia-Aymerich; PAC-COPD Study Group, Association between Ω3 and Ω6 fatty acid intakes and serum inflammatory markers in COPD. *J. Nutr. Biochem.* **23**, 817–821 (2012). doi:10.1016/j.jnutbio.2011.04.005 Medline

38. P. C. Calder, Polyunsaturated fatty acids and inflammatory processes: New twists in an old tale. *Biochimie* **91**, 791–795 (2009). doi:10.1016/j.biochi.2009.01.008 Medline

39. Human Microbiome Project Consortium, Structure, function and diversity of the healthy human microbiome. *Nature* **486**, 207–214 (2012). doi:10.1038/nature11234 Medline

40. S. Li, S. W. Tighe, C. M. Nicolet, D. Grove, S. Levy, W. Farmerie, A. Viale, C. Wright, P. A. Schweitzer, Y. Gao, D. Kim, J. Boland, B. Hicks, R. Kim, S. Chhangawala, N. Jafari, N. Raghavachari, J. Gandara, N. Garcia-Reyero, C. Hendrickson, D. Roberson, J. A. Rosenfeld, T. Smith, J. G. Underwood, M. Wang, P. Zumbo, D. A. Baldwin, G. S. Grills, C. E. Mason, Multi-platform assessment of transcriptome profiling using RNA-seq in the ABRF next-generation sequencing study. *Nat. Biotechnol.* **32**, 915–925 (2014). doi:10.1038/nbt.2972 Medline

41. SEQC/MAQC-III Consortium, A comprehensive assessment of RNA-seq accuracy, reproducibility and information content by the Sequencing Quality Control Consortium. *Nat. Biotechnol.* **32**, 903–914 (2014). doi:10.1038/nbt.2957 Medline

42. C. M. Gardiner, D. K. Finlay, What fuels natural killers? Metabolism and NK cell responses. *Front. Immunol.* **8**, 367 (2017). doi:10.3389/fimmu.2017.00367 Medline

43. A. Beheshti, E. Cekanaviciute, D. J. Smith, S. V. Costes, Global transcriptomic analysis suggests carbon dioxide as an environmental stressor in spaceflight: A systems biology GeneLab case study. *Sci. Rep.* **8**, 4191 (2018). doi:10.1038/s41598-018-22613-1 Medline

44. P. Norsk, A. Asmar, M. Damgaard, N. J. Christensen, Fluid shifts, vasodilatation and ambulatory blood pressure reduction during long duration spaceflight. *J. Physiol.* **593**, 573–584 (2015). doi:10.1113/jphysiol.2014.284869 Medline

45. P. Arbeille, R. Provost, K. Zuj, Carotid and femoral artery intima-media thickness during 6 months of spaceflight. *Aerosp. Med. Hum. Perform.* **87**, 449–453 (2016). doi:10.3357/AMHP.4493.2016 Medline

46. S. R. Zwart, R. D. Launius, G. K. Coen, J. L. L. Morgan, J. B. Charles, S. M. Smith, Body mass changes during long-duration spaceflight. *Aviat. Space Environ. Med.* **85**, 897–904 (2014). doi:10.3357/ASEM.3979.2014 Medline

47. S. M. Smith, M. Heer, L. C. Shackelford, J. D. Sibonga, J. Spatz, R. A. Pietrzyk, E. K. Hudson, S. R. Zwart, Bone metabolism and renal stone risk during International Space Station missions. *Bone* **81**, 712–720 (2015). doi:10.1016/j.bone.2015.10.002 Medline

48. S. M. Smith, S. A. Abrams, J. E. Davis-Street, M. Heer, K. O. O'Brien, M. E. Wastney, S. R. Zwart, Fifty years of human space travel: Implications for bone and calcium research. *Annu. Rev. Nutr.* **34**, 377–400 (2014). doi:10.1146/annurev-nutr-071813-105440 Medline

49. X. Wang, S. Abraham, J. A. G. McKenzie, N. Jeffs, M. Swire, V. B. Tripathi, U. F. O. Luhmann, C. A. K. Lange, Z. Zhai, H. M. Arthur, J. Bainbridge, S. E. Moss, J. Greenwood, LRG1 promotes angiogenesis by modulating endothelial TGF-β signalling. *Nature* **499**, 306–311 (2013). doi:10.1038/nature12345 Medline

50. S. R. Zwart, J. F. Gregory, S. H. Zeisel, C. R. Gibson, T. H. Mader, J. M. Kinchen, P. M. Ueland, R. Ploutz-Snyder, M. A. Heer, S. M. Smith, Genotype, B-vitamin status, and androgens affect spaceflight-induced ophthalmic changes. *FASEB J.* **30**, 141–148 (2016). doi:10.1096/fj.15-278457 Medline

51. S. R. Zwart, C. R. Gibson, T. H. Mader, K. Ericson, R. Ploutz-Snyder, M. Heer, S. M. Smith, Vision changes after spaceflight are related to alterations in folate- and vitamin B-12-dependent one-carbon metabolism. *J. Nutr.* **142**, 427–431 (2012). doi:10.3945/jn.111.154245 Medline

52. M. Basner, A. Savitt, T. M. Moore, A. M. Port, S. McGuire, A. J. Ecker, J. Nasrini, D. J. Mollicone, C. M. Mott, T. McCann, D. F. Dinges, R. C. Gur, Development and validation of the cognition test battery for spaceflight. *Aerosp. Med. Hum. Perform.* **86**, 942–952 (2015). doi:10.3357/AMHP.4343.2015 Medline

53. Y. Zhao, K. Lai, I. Cheung, J. Youds, M. Tarailo, S. Tarailo, A. Rose, A mutational analysis of *Caenorhabditis elegans* in space. *Mutat. Res.* **601**, 19–29 (2006). doi:10.1016/j.mrfmmm.2006.05.001 Medline

54. M. A. Shammas, Telomeres, lifestyle, cancer, and aging. *Curr. Opin. Clin. Nutr. Metab. Care* **14**, 28–34 (2011). doi:10.1097/MCO.0b013e32834121b1 Medline

55. W. R. Pendergrass, P. E. Penn, J. Li, N. S. Wolf, Age-related telomere shortening occurs in lens epithelium from old rats and is slowed by caloric restriction. *Exp. Eye Res.* **73**, 221–228 (2001). doi:10.1006/exer.2001.1033 Medline

56. M. Laimer, A. Melmer, C. Lamina, J. Raschenberger, P. Adamovski, J. Engl, C. Ress, A. Tschoner, C. Gelsinger, L. Mair, S. Kiechl, J. Willeit, P. Willeit, C. Stettler, H. Tilg, F. Kronenberg, C. Ebenbichler, Telomere length increase after weight loss induced by bariatric surgery: Results from a 10 year prospective study. *Int. J. Obes.* **40**, 773–778 (2016). doi:10.1038/ijo.2015.238 Medline

57. L. F. Cherkas, J. L. Hunkin, B. S. Kato, J. B. Richards, J. P. Gardner, G. L. Surdulescu, M. Kimura, X. Lu, T. D. Spector, A. Aviv, The association between physical activity in leisure time and leukocyte telomere length. *Arch. Intern. Med.* **168**, 154–158 (2008). doi:10.1001/archinternmed.2007.39 Medline

58. L. Carulli, C. Anzivino, E. Baldelli, M. F. Zenobii, M. B. L. Rocchi, M. Bertolotti, Telomere length elongation after weight loss intervention in obese adults. *Mol. Genet. Metab.* **118**, 138–142 (2016). doi:10.1016/j.ymgme.2016.04.003 Medline

59. V. Boccardi, G. Paolisso, P. Mecocci, Nutrition and lifestyle in healthy aging: The telomerase challenge. *Aging* **8**, 12–15 (2016). doi:10.18632/aging.100886 Medline

60. N. C. Arsenis, T. You, E. F. Ogawa, G. M. Tinsley, L. Zuo, Physical activity and telomere length: Impact of aging and potential mechanisms of action. *Oncotarget* **8**, 45008–45019 (2017). doi:10.18632/oncotarget.16726 Medline

61. S. Turroni, S. Rampelli, E. Biagi, C. Consolandi, M. Severgnini, C. Peano, S. Quercia, M. Soverini, F. G. Carbonero, G. Bianconi, P. Rettberg, F. Canganella, P. Brigidi, M. Candela, Temporal dynamics of the gut microbiota in people sharing a confined environment, a 520-day ground-based space simulation, MARS500. *Microbiome* **5**, 39 (2017). doi:10.1186/s40168-017-0256-8 Medline

62. A. V. Mardanov, M. M. Babykin, A. V. Beletsky, A. I. Grigoriev, V. V. Zinchenko, V. V. Kadnikov, M. P. Kirpichnikov, A. M. Mazur, A. V. Nedoluzhko, N. D. Novikova, E. B. Prokhortchouk, N. V. Ravin, K. G. Skryabin, S. V. Shestakov, Metagenomic analysis of the dynamic changes in the gut microbiome of the participants of the MARS-500 experiment, simulating long term space flight. *Acta Naturae* **5**, 116–125 (2013). Medline

63. M. J. Mienaltowski, D. E. Birk, Structure, physiology, and biochemistry of collagens. *Adv. Exp. Med. Biol.* **802**, 5–29 (2014). doi:10.1007/978-94-007-7893-1_2 Medline

64. S. Sasaki, Aquaporin 2: From its discovery to molecular structure and medical implications. *Mol. Aspects Med.* **33**, 535–546 (2012). doi:10.1016/j.mam.2012.03.004 Medline

65. H. Yamada, D. Chen, H. J. Monstein, R. Håkanson, Effects of fasting on the expression of gastrin, cholecystokinin, and somatostatin genes and of various housekeeping genes in the pancreas and upper digestive tract of rats. *Biochem. Biophys. Res. Commun.* **231**, 835–838 (1997). doi:10.1006/bbrc.1997.6198 Medline

66. A. Nguyen Dinh Cat, R. M. Touyz, A new look at the renin-angiotensin system—Focusing on the vascular system. *Peptides* **32**, 2141–2150 (2011). doi:10.1016/j.peptides.2011.09.010 Medline

67. F. S. Michel, G. R. Norton, M. J. Maseko, O. H. I. Majane, P. Sareli, A. J. Woodiwiss, Urinary angiotensinogen excretion is associated with blood pressure independent of the circulating renin-angiotensin system in a group of African ancestry. *Hypertension* **64**, 149–156 (2014). doi:10.1161/HYPERTENSIONAHA.114.03336 Medline

68. J. Zhang, G. Rane, X. Dai, M. K. Shanmugam, F. Arfuso, R. P. Samy, M. K. P. Lai, D. Kappei, A. P. Kumar, G. Sethi, Ageing and the telomere connection: An intimate relationship with inflammation. *Ageing Res. Rev.* **25**, 55–69 (2016). doi:10.1016/j.arr.2015.11.006 Medline

69. R. C. Stone, K. Horvath, J. D. Kark, E. Susser, S. A. Tishkoff, A. Aviv, Telomere length and the cancer-atherosclerosis trade-off. *PLOS Genet.* **12**, e1006144 (2016). doi:10.1371/journal.pgen.1006144 Medline

70. B. E. Crucian, A. Choukèr, R. J. Simpson, S. Mehta, G. Marshall, S. M. Smith, S. R. Zwart, M. Heer, S. Ponomarev, A. Whitmire, J. P. Frippiat, G. L. Douglas, H. Lorenzi, J.-I. Buchheim, G. Makedonas, G. S. Ginsburg, C. M. Ott, D. L. Pierson, S. S. Krieger, N. Baecker, C. Sams, Immune system dysregulation during spaceflight: Potential countermeasures for deep space exploration missions. *Front. Immunol.* **9**, 1437 (2018). doi:10.3389/fimmu.2018.01437 Medline

71. T. H. Mader, C. R. Gibson, A. F. Pass, A. G. Lee, H. E. Killer, H.-C. Hansen, J. P. Dervay, M. R. Barratt, W. J. Tarver, A. E. Sargsyan, L. A. Kramer, R. Riascos, D. G. Bedi, D. R. Pettit, Optic disc edema in an astronaut after repeat long-duration space flight. *J. Neuroophthalmol.* **33**, 249–255 (2013). doi:10.1097/WNO.0b013e31829b41a6 Medline

72. S. R. Zwart, C. R. Gibson, J. F. Gregory, T. H. Mader, P. J. Stover, S. H. Zeisel, S. M. Smith, Astronaut ophthalmic syndrome. *FASEB J.* **31**, 3746–3756 (2017). doi:10.1096/fj.201700294 Medline

73. P. Arbeille, R. Provost, K. Zuj, N. Vincent, Measurements of jugular, portal, femoral, and calf vein cross-sectional area for the assessment of venous blood redistribution with long duration spaceflight (Vessel Imaging Experiment). *Eur. J. Appl. Physiol.* **115**, 2099–2106 (2015). doi:10.1007/s00421-015-3189-6 Medline

74. R. L. Hughson, A. D. Robertson, P. Arbeille, J. K. Shoemaker, J. W. E. Rush, K. S. Fraser, D. K. Greaves, Increased postflight carotid artery stiffness and inflight insulin resistance resulting from 6-mo spaceflight in male and female astronauts. *Am. J. Physiol. Heart Circ. Physiol.* **310**, H628–H638 (2016). doi:10.1152/ajpheart.00802.2015 Medline

75. M. W. Lorenz, H. S. Markus, M. L. Bots, M. Rosvall, M. Sitzer, Prediction of clinical cardiovascular events with carotid intima-media thickness: A systematic review and meta-analysis. *Circulation* **115**, 459–467 (2007). doi:10.1161/CIRCULATIONAHA.106.628875 Medline

76. G. Walldius, I. Jungner, The apoB/apoA-I ratio: A strong, new risk factor for cardiovascular disease and a target for lipid-lowering therapy—a review of the evidence. *J. Intern. Med.* **259**, 493–519 (2006). doi:10.1111/j.1365-2796.2006.01643.x Medline

77. G. Florvall, S. Basu, A. Larsson, Apolipoprotein A1 is a stronger prognostic marker than are HDL and LDL cholesterol for cardiovascular disease and mortality in elderly men. *J. Gerontol. A Biol. Sci. Med. Sci.* **61**, 1262–1266 (2006). doi:10.1093/gerona/61.12.1262 Medline

78. M. Benn, B. G. Nordestgaard, G. B. Jensen, A. Tybjaerg-Hansen, Improving prediction of ischemic cardiovascular disease in the general population using apolipoprotein B: The Copenhagen City Heart Study. *Arterioscler. Thromb. Vasc. Biol.* **27**, 661–670 (2007). doi:10.1161/01.ATV.0000255580.73689.8e Medline

79. C. J. Ade, R. M. Broxterman, J. M. Charvat, T. J. Barstow, Incidence rate of cardiovascular disease end points in the National Aeronautics and Space Administration Astronaut Corps. *J. Am. Heart Assoc.* **6**, e005564 (2017). doi:10.1161/JAHA.117.005564 Medline

80. R. J. Reynolds, S. M. Day, Mortality among U.S. astronauts: 1980–2009. *Aviat. Space Environ. Med.* **81**, 1024–1027 (2010). doi:10.3357/ASEM.2847.2010 Medline

81. A. P. Mulavara, B. T. Peters, C. A. Miller, I. S. Kofman, M. F. Reschke, L. C. Taylor, E. L. Lawrence, S. J. Wood, S. S. Laurie, S. M. C. Lee, R. E. Buxton, T. R. May-Phillips, M. B. Stenger, L. L. Ploutz-Snyder, J. W. Ryder, A. H. Feiveson, J. J. Bloomberg, Physiological and functional alterations after spaceflight and bed rest. *Med. Sci. Sports Exerc.* **50**, 1961–1980 (2018). doi:10.1249/MSS.0000000000001615 Medline

82. S. Behjati, G. Gundem, D. C. Wedge, N. D. Roberts, P. S. Tarpey, S. L. Cooke, P. Van Loo, L. B. Alexandrov, M. Ramakrishna, H. Davies, S. Nik-Zainal, C. Hardy, C. Latimer, K. M. Raine, L. Stebbings, A. Menzies, D. Jones, R. Shepherd, A. P. Butler, J. W. Teague, M. Jorgensen, B. Khatri, N. Pillay, A. Shlien, P. A. Futreal, C. Badie, U. McDermott, G. S. Bova, A. L. Richardson, A. M. Flanagan, M. R. Stratton, P. J. Campbell; ICGC Prostate Group, Mutational signatures of ionizing radiation in second malignancies. *Nat. Commun.* **7**, 12605 (2016). doi:10.1038/ncomms12605 Medline

83. F. Berardinelli, A. Antoccia, R. Buonsante, S. Gerardi, R. Cherubini, V. De Nadal, C. Tanzarella, A. Sgura, The role of telomere length modulation in delayed chromosome instability induced by ionizing radiation in human primary fibroblasts. *Environ. Mol. Mutagen.* **54**, 172–179 (2013). doi:10.1002/em.21761 Medline

84. F. A. Cucinotta, N. Hamada, M. P. Little, No evidence for an increase in circulatory disease mortality in astronauts following space radiation exposures. *Life Sci. Space Res.* **10**, 53–56 (2016). doi:10.1016/j.lssr.2016.08.002 Medline

85. J. T. Leek, W. E. Johnson, H. S. Parker, A. E. Jaffe, J. D. Storey, The sva package for removing batch effects and other unwanted variation in high-throughput experiments. *Bioinformatics* **28**, 882–883 (2012). doi:10.1093/bioinformatics/bts034 Medline

86. ACK lysis buffer. *Cold Spring Harb. Protoc.* **2014**, pdb.rec083295 (2014). doi:10.1101/pdb.rec083295

87. E. S. Williams, M. N. Cornforth, E. H. Goodwin, S. M. Bailey, CO-FISH, COD-FISH, ReD-FISH, SKY-FISH. *Methods Mol. Biol.* **735**, 113–124 (2011). doi:10.1007/978-1-61779-092-8_11 Medline

88. K. J. Livak, T. D. Schmittgen, Analysis of relative gene expression data using real-time quantitative PCR and the $2^{-\Delta\Delta CT}$ method. *Methods* **25**, 402–408 (2001). doi:10.1006/meth.2001.1262 Medline

89. H. P. Wong, P. Slijepcevic, Telomere length measurement in mouse chromosomes by a modified Q-FISH method. *Cytogenet. Genome Res.* **105**, 464–470 (2004). doi:10.1159/000078220 Medline

90. F. Krueger, S. R. Andrews, Bismark: A flexible aligner and methylation caller for Bisulfite-Seq applications. *Bioinformatics* **27**, 1571–1572 (2011). doi:10.1093/bioinformatics/btr167 Medline

91. K. D. Hansen, B. Langmead, R. A. Irizarry, BSmooth: From whole genome bisulfite sequencing reads to differentially methylated regions. *Genome Biol.* **13**, R83 (2012). doi:10.1186/gb-2012-13-10-r83 Medline

92. G. Jenkinson, J. Abante, A. P. Feinberg, J. Goutsias, An information-theoretic approach to the modeling and analysis of whole-genome bisulfite sequencing data. *BMC Bioinformatics* **19**, 87 (2018). doi:10.1186/s12859-018-2086-5 Medline

93. R. Breitling, P. Armengaud, A. Amtmann, P. Herzyk, Rank products: A simple, yet powerful, new method to detect differentially regulated genes in replicated microarray experiments. *FEBS Lett.* **573**, 83–92 (2004). doi:10.1016/j.febslet.2004.07.055 Medline

94. E. Eden, R. Navon, I. Steinfeld, D. Lipson, Z. Yakhini, GOrilla: A tool for discovery and visualization of enriched GO terms in ranked gene lists. *BMC Bioinformatics* **10**, 48 (2009). doi:10.1186/1471-2105-10-48 Medline

95. E. Eden, D. Lipson, S. Yogev, Z. Yakhini, Discovering motifs in ranked lists of DNA sequences. *PLOS Comput. Biol.* **3**, e39 (2007). doi:10.1371/journal.pcbi.0030039 Medline

96. P. Ewels, M. Magnusson, S. Lundin, M. Käller, MultiQC: Summarize analysis results for multiple tools and samples in a single report. *Bioinformatics* **32**, 3047–3048 (2016). doi:10.1093/bioinformatics/btw354 Medline

97. S. Andrews, FastQC: A quality control tool for high throughput sequence data (2010); www.bioinformatics.babraham.ac.uk/projects/fastqc/.

98. F. Krueger, Trim Galore (2016); www.bioinformatics.babraham.ac.uk/projects/trim_galore/.

99. M. Martin, Cutadapt removes adapter sequences from high-throughput sequencing reads. *EMBnet.journal* **17**, 10–12 (2011). doi:10.14806/ej.17.1.200

100. J. Harrow, A. Frankish, J. M. Gonzalez, E. Tapanari, M. Diekhans, F. Kokocinski, B. L. Aken, D. Barrell, A. Zadissa, S. Searle, I. Barnes, A. Bignell, V. Boychenko, T. Hunt, M. Kay, G. Mukherjee, J. Rajan, G. Despacio-Reyes, G. Saunders, C. Steward, R. Harte, M. Lin, C. Howald, A. Tanzer, T. Derrien, J. Chrast, N. Walters, S. Balasubramanian, B. Pei, M. Tress, J. M. Rodriguez, I. Ezkurdia, J. van Baren, M. Brent, D. Haussler, M. Kellis, A. Valencia, A. Reymond, M. Gerstein, R. Guigó, T. J. Hubbard, GENCODE: The reference human genome annotation for The ENCODE Project. *Genome Res.* **22**, 1760–1774 (2012). doi:10.1101/gr.135350.111 Medline

101. A. Dobin, C. A. Davis, F. Schlesinger, J. Drenkow, C. Zaleski, S. Jha, P. Batut, M. Chaisson, T. R. Gingeras, STAR: Ultrafast universal RNA-seq aligner. *Bioinformatics* **29**, 15–21 (2013). doi:10.1093/bioinformatics/bts635 Medline

102. D. R. Zerbino, P. Achuthan, W. Akanni, M. R. Amode, D. Barrell, J. Bhai, K. Billis, C. Cummins, A. Gall, C. G. Girón, L. Gil, L. Gordon, L. Haggerty, E. Haskell, T. Hourlier, O. G. Izuogu, S. H. Janacek, T. Juettemann, J. K. To, M. R. Laird, I. Lavidas, Z. Liu, J. E. Loveland, T. Maurel, W. McLaren, B. Moore, J. Mudge, D. N. Murphy, V. Newman, M. Nuhn, D. Ogeh, C. K. Ong, A. Parker, M. Patricio, H. S. Riat, H. Schuilenburg, D. Sheppard, H. Sparrow, K. Taylor, A. Thormann, A. Vullo, B. Walts, A. Zadissa, A. Frankish, S. E. Hunt, M. Kostadima, N. Langridge, F. J. Martin, M. Muffato, E. Perry, M. Ruffier, D. M. Staines, S. J. Trevanion, B. L. Aken, F. Cunningham, A. Yates, P. Flicek, Ensembl 2018. *Nucleic Acids Res.* **46** (D1), D754–D761 (2018). doi:10.1093/nar/gkx1098 Medline

103. Y. Liao, G. K. Smyth, W. Shi, featureCounts: An efficient general purpose program for assigning sequence reads to genomic features. *Bioinformatics* **30**, 923–930 (2014). doi:10.1093/bioinformatics/btt656 Medline

104. N. L. Bray, H. Pimentel, P. Melsted, L. Pachter, Near-optimal probabilistic RNA-seq quantification. *Nat. Biotechnol.* **34**, 525–527 (2016). doi:10.1038/nbt.3519 Medline

105. M. I. Love, W. Huber, S. Anders, Moderated estimation of fold change and dispersion for RNA-seq data with DESeq2. *Genome Biol.* **15**, 550 (2014). doi:10.1186/s13059-014-0550-8 Medline

106. A. Subramanian, P. Tamayo, V. K. Mootha, S. Mukherjee, B. L. Ebert, M. A. Gillette, A. Paulovich, S. L. Pomeroy, T. R. Golub, E. S. Lander, J. P. Mesirov, Gene set enrichment analysis: A knowledge-based approach for interpreting genome-wide expression profiles. *Proc. Natl. Acad. Sci. U.S.A.* **102**, 15545–15550 (2005). doi:10.1073/pnas.0506580102 Medline

107. C. L. Smith, J. A. Blake, J. A. Kadin, J. E. Richardson, C. J. Bult; Mouse Genome Database Group, Mouse Genome Database (MGD)-2018: Knowledgebase for the laboratory mouse. *Nucleic Acids Res.* **46** (D1), D836–D842 (2018). doi:10.1093/nar/gkx1006 Medline

108. A. Liberzon, A. Subramanian, R. Pinchback, H. Thorvaldsdóttir, P. Tamayo, J. P. Mesirov, Molecular signatures database (MSigDB) 3.0. *Bioinformatics* **27**, 1739–1740 (2011). doi:10.1093/bioinformatics/btr260 Medline

109. A. Sergushichev, An algorithm for fast preranked gene set enrichment analysis using cumulative statistic calculation. bioRxiv 060012 [Preprint]. 20 June 2016. https://doi.org/10.1101/060012v1.

110. M. D. Robinson, A. Oshlack, A scaling normalization method for differential expression analysis of RNA-seq data. *Genome Biol.* **11**, R25 (2010). doi:10.1186/gb-2010-11-3-r25 Medline

111. J. T. Leek, W. E. Johnson, H. S. Parker, E. J. Fertig, A. E. Jaffe, J. D. Storey, sva: Surrogate Variable Analysis, R Package version 3.20.0 (2016).

112. W. E. Johnson, C. Li, A. Rabinovic, Adjusting batch effects in microarray expression data using empirical Bayes methods. *Biostatistics* **8**, 118–127 (2007). doi:10.1093/biostatistics/kxj037 Medline

113. V. Nygaard, E. A. Rødland, E. Hovig, Methods that remove batch effects while retaining group differences may lead to exaggerated confidence in downstream analyses. *Biostatistics* **17**, 29–39 (2016). Medline

114. L. V. D. Maaten, G. Hinton, Visualizing data using t-SNE. *J. Mach. Learn. Res.* **9**, 2579–2605 (2008).

115. C. Wang, C. M. Sanders, Q. Yang, H. W. Schroeder Jr., E. Wang, F. Babrzadeh, B. Gharizadeh, R. M. Myers, J. R. Hudson Jr., R. W. Davis, J. Han, High throughput sequencing reveals a complex pattern of dynamic interrelationships among human T cell subsets. *Proc. Natl. Acad. Sci. U.S.A.* **107**, 1518–1523 (2010). doi:10.1073/pnas.0913939107 Medline

116. T. Magoč, S. L. Salzberg, FLASH: Fast length adjustment of short reads to improve genome assemblies. *Bioinformatics* **27**, 2957–2963 (2011). doi:10.1093/bioinformatics/btr507 Medline

117. S. F. Altschul, W. Gish, W. Miller, E. W. Myers, D. J. Lipman, Basic local alignment search tool. *J. Mol. Biol.* **215**, 403–410 (1990). doi:10.1016/S0022-2836(05)80360-2 Medline

118. B. MacLean, D. M. Tomazela, N. Shulman, M. Chambers, G. L. Finney, B. Frewen, R. Kern, D. L. Tabb, D. C. Liebler, M. J. MacCoss, Skyline: An open source document editor for creating and analyzing targeted proteomics experiments. *Bioinformatics* **26**, 966–968 (2010). doi:10.1093/bioinformatics/btq054 Medline

119. Y. S. Ting, J. D. Egertson, J. G. Bollinger, B. C. Searle, S. H. Payne, W. S. Noble, M. J. MacCoss, PECAN: Library-free peptide detection for data-independent acquisition tandem mass spectrometry data. *Nat. Methods* **14**, 903–908 (2017). doi:10.1038/nmeth.4390 Medline

120. B. C. Searle, L. K. Pino, J. D. Egertson, Y. S. Ting, R. T. Lawrence, B. X. MacLean, J. Villén, M. J. MacCoss, Chromatogram libraries improve peptide detection and quantification by data

independent acquisition mass spectrometry. *Nat. Commun.* **9**, 5128 (2018). doi:10.1038/s41467-018-07454-w Medline

121. G. Teo, S. Kim, C.-C. Tsou, B. Collins, A.-C. Gingras, A. I. Nesvizhskii, H. Choi, mapDIA: Preprocessing and statistical analysis of quantitative proteomics data from data independent acquisition mass spectrometry. *J. Proteomics* **129**, 108–120 (2015). doi:10.1016/j.jprot.2015.09.013 Medline

122. D. W. Huang, B. T. Sherman, Q. Tan, J. R. Collins, W. G. Alvord, J. Roayaei, R. Stephens, M. W. Baseler, H. C. Lane, R. A. Lempicki, The DAVID Gene Functional Classification Tool: A novel biological module-centric algorithm to functionally analyze large gene lists. *Genome Biol.* **8**, R183 (2007). doi:10.1186/gb-2007-8-9-r183 Medline

123. B. D. Piening, W. Zhou, K. Contrepois, H. Röst, G. J. Gu Urban, T. Mishra, B. M. Hanson, E. J. Bautista, S. Leopold, C. Y. Yeh, D. Spakowicz, I. Banerjee, C. Chen, K. Kukurba, D. Perelman, C. Craig, E. Colbert, D. Salins, S. Rego, S. Lee, C. Zhang, J. Wheeler, M. R. Sailani, L. Liang, C. Abbott, M. Gerstein, A. Mardinoglu, U. Smith, D. L. Rubin, S. Pitteri, E. Sodergren, T. L. McLaughlin, G. M. Weinstock, M. P. Snyder, Integrative personal omics profiles during periods of weight gain and loss. *Cell Syst.* **6**, 157–170.e8 (2018). doi:10.1016/j.cels.2017.12.013 Medline

124. K. Nakahira, S.-Y. Kyung, A. J. Rogers, L. Gazourian, S. Youn, A. F. Massaro, C. Quintana, J. C. Osorio, Z. Wang, Y. Zhao, L. A. Lawler, J. D. Christie, N. J. Meyer, F. R. Mc Causland, S. S. Waikar, A. B. Waxman, R. T. Chung, R. Bueno, I. O. Rosas, L. E. Fredenburgh, R. M. Baron, D. C. Christiani, G. M. Hunninghake, A. M. K. Choi, Circulating mitochondrial DNA in patients in the ICU as a marker of mortality: Derivation and validation. *PLOS Med.* **10**, e1001577, discussion e1001577 (2013). doi:10.1371/journal.pmed.1001577 Medline

125. S. M. Smith, M. Heer, Z. Wang, C. L. Huntoon, S. R. Zwart, Long-duration space flight and bed rest effects on testosterone and other steroids. *J. Clin. Endocrinol. Metab.* **97**, 270–278 (2012). doi:10.1210/jc.2011-2233 Medline

126. B. E. Crucian, S. R. Zwart, S. Mehta, P. Uchakin, H. D. Quiriarte, D. Pierson, C. F. Sams, S. M. Smith, Plasma cytokine concentrations indicate that in vivo hormonal regulation of immunity is altered during long-duration spaceflight. *J. Interferon Cytokine Res.* **34**, 778–786 (2014). doi:10.1089/jir.2013.0129 Medline

127. B. R. Soller, M. Cabrera, S. M. Smith, J. P. Sutton, Smart medical systems with application to nutrition and fitness in space. *Nutrition* **18**, 930–936 (2002). doi:10.1016/S0899-9007(02)00897-3 Medline

128. S. M. Smith, J. E. Davis-Street, B. L. Rice, J. L. Nillen, P. L. Gillman, G. Block, Nutritional status assessment in semiclosed environments: Ground-based and space flight studies in humans. *J. Nutr.* **131**, 2053–2061 (2001). doi:10.1093/jn/131.7.2053 Medline

129. S. S. Laurie, G. Vizzeri, G. Taibbi, C. R. Ferguson, X. Hu, S. M. C. Lee, R. Ploutz-Snyder, S. M. Smith, S. R. Zwart, M. B. Stenger, Effects of short-term mild hypercapnia during head-down tilt on intracranial pressure and ocular structures in healthy human subjects. *Physiol. Rep.* **5**, e13302 (2017). doi:10.14814/phy2.13302 Medline

130. T. M. Moore, S. P. Reise, R. E. Gur, H. Hakonarson, R. C. Gur, Psychometric properties of the Penn Computerized Neurocognitive Battery. *Neuropsychology* **29**, 235–246 (2015). doi:10.1037/neu0000093 Medline

131. R. C. Gur, J. Richard, P. Hughett, M. E. Calkins, L. Macy, W. B. Bilker, C. Brensinger, R. E. Gur, A cognitive neuroscience-based computerized battery for efficient measurement of individual

differences: Standardization and initial construct validation. *J. Neurosci. Methods* **187**, 254–262 (2010). doi:10.1016/j.jneumeth.2009.11.017 Medline

132. R. C. Gur, J. Richard, M. E. Calkins, R. Chiavacci, J. A. Hansen, W. B. Bilker, J. Loughead, J. J. Connolly, H. Qiu, F. D. Mentch, P. M. Abou-Sleiman, H. Hakonarson, R. E. Gur, Age group and sex differences in performance on a computerized neurocognitive battery in children age 8–21. *Neuropsychology* **26**, 251–265 (2012). doi:10.1037/a0026712 Medline

133. N. Usui, T. Haji, M. Maruyama, N. Katsuyama, S. Uchida, A. Hozawa, K. Omori, I. Tsuji, R. Kawashima, M. Taira, Cortical areas related to performance of WAIS Digit Symbol Test: A functional imaging study. *Neurosci. Lett.* **463**, 1–5 (2009). doi:10.1016/j.neulet.2009.07.048 Medline

134. J. Lim, D. F. Dinges, Sleep deprivation and vigilant attention. *Ann. N. Y. Acad. Sci.* **1129**, 305–322 (2008). doi:10.1196/annals.1417.002 Medline

135. D. R. Roalf, K. Ruparel, R. E. Gur, W. Bilker, R. Gerraty, M. A. Elliott, R. S. Gallagher, L. Almasy, M. F. Pogue-Geile, K. Prasad, J. Wood, V. L. Nimgaonkar, R. C. Gur, Neuroimaging predictors of cognitive performance across a standardized neurocognitive battery. *Neuropsychology* **28**, 161–176 (2014). doi:10.1037/neu0000011 Medline

136. T. M. Moore, M. Basner, J. Nasrini, E. Hermosillo, S. Kabadi, D. R. Roalf, S. McGuire, A. J. Ecker, K. Ruparel, A. M. Port, C. T. Jackson, D. F. Dinges, R. C. Gur, Validation of the Cognition Test Battery for spaceflight in a sample of highly educated adults. *Aerosp. Med. Hum. Perform.* **88**, 937–946 (2017). doi:10.3357/AMHP.4801.2017 Medline

137. R. C. Gur, J. D. Ragland, P. J. Moberg, T. H. Turner, W. B. Bilker, C. Kohler, S. J. Siegel, R. E. Gur, Computerized neurocognitive scanning: I. Methodology and validation in healthy people. *Neuropsychopharmacology* **25**, 766–776 (2001). doi:10.1016/S0893-133X(01)00278-0 Medline

138. D. C. Glahn, R. C. Gur, J. D. Ragland, D. M. Censits, R. E. Gur, Reliability, performance characteristics, construct validity, and an initial clinical application of a visual object learning test (VOLT). *Neuropsychology* **11**, 602–612 (1997). doi:10.1037/0894-4105.11.4.602 Medline

139. J. D. Ragland, B. I. Turetsky, R. C. Gur, F. Gunning-Dixon, T. Turner, L. Schroeder, R. Chan, R. E. Gur, Working memory for complex figures: An fMRI comparison of letter and fractal *n*-back tasks. *Neuropsychology* **16**, 370–379 (2002). doi:10.1037/0894-4105.16.3.370 Medline

140. D. C. Glahn, T. D. Cannon, R. E. Gur, J. D. Ragland, R. C. Gur, Working memory constrains abstraction in schizophrenia. *Biol. Psychiatry* **47**, 34–42 (2000). doi:10.1016/S0006-3223(99)00187-0 Medline

141. A. L. Benton, N. R. Varney, K. D. Hamsher, Visuospatial judgment. A clinical test. *Arch. Neurol.* **35**, 364–367 (1978). doi:10.1001/archneur.1978.00500300038006 Medline

142. J. C. Raven, *Advanced Progressive Matrices Sets I and II* (Lewis, London, 1965).

143. B. Perfetti, A. Saggino, A. Ferretti, M. Caulo, G. L. Romani, M. Onofrj, Differential patterns of cortical activation as a function of fluid reasoning complexity. *Hum. Brain Mapp.* **30**, 497–510 (2009). doi:10.1002/hbm.20519 Medline

144. C. W. Lejuez, J. P. Read, C. W. Kahler, J. B. Richards, S. E. Ramsey, G. L. Stuart, D. R. Strong, R. A. Brown, Evaluation of a behavioral measure of risk taking: The Balloon Analogue Risk Task (BART). *J. Exp. Psychol. Appl.* **8**, 75–84 (2002). doi:10.1037/1076-898X.8.2.75 Medline

145. M. Basner, D. Mollicone, D. F. Dinges, Validity and sensitivity of a brief Psychomotor Vigilance Test (PVT-B) to total and partial sleep deprivation. *Acta Astronaut.* **69**, 949–959 (2011). doi:10.1016/j.actaastro.2011.07.015 Medline

146. L. K. Barger, E. E. Flynn-Evans, A. Kubey, L. Walsh, J. M. Ronda, W. Wang, K. P. Wright Jr., C. A. Czeisler, Prevalence of sleep deficiency and use of hypnotic drugs in astronauts before, during, and after spaceflight: An observational study. *Lancet Neurol.* **13**, 904–912 (2014). doi:10.1016/S1474-4422(14)70122-X Medline

147. M. Basner, E. Hermosillo, J. Nasrini, S. McGuire, S. Saxena, T. M. Moore, R. C. Gur, D. F. Dinges, Repeated administration effects on Psychomotor Vigilance Test performance. *Sleep* **41**, 1–6 (2018). Medline

148. D. F. Dinges, An overview of sleepiness and accidents. *J. Sleep Res.* **4** (S2), 4–14 (1995). doi:10.1111/j.1365-2869.1995.tb00220.x Medline

149. B. Buchfink, C. Xie, D. H. Huson, Fast and sensitive protein alignment using DIAMOND. *Nat. Methods* **12**, 59–60 (2015). doi:10.1038/nmeth.3176 Medline

150. D. H. Huson, A. F. Auch, J. Qi, S. C. Schuster, MEGAN analysis of metagenomic data. *Genome Res.* **17**, 377–386 (2007). doi:10.1101/gr.5969107 Medline

151. G. G. Silva, K. T. Green, B. E. Dutilh, R. A. Edwards, SUPER-FOCUS: A tool for agile functional analysis of shotgun metagenomic data. *Bioinformatics* **32**, 354–361 (2016). doi:10.1093/bioinformatics/btv584 Medline

152. M. D. Robinson, D. J. McCarthy, G. K. Smyth, edgeR: A Bioconductor package for differential expression analysis of digital gene expression data. *Bioinformatics* **26**, 139–140 (2010). doi:10.1093/bioinformatics/btp616 Medline

153. D. J. McCarthy, Y. Chen, G. K. Smyth, Differential expression analysis of multifactor RNA-Seq experiments with respect to biological variation. *Nucleic Acids Res.* **40**, 4288–4297 (2012). doi:10.1093/nar/gks042 Medline

154. Y. Benjamini, Y. Hochberg, Controlling the false discovery rate: A practical and powerful approach to multiple testing. *J. R. Stat. Soc. B* **57**, 289–300 (1995). doi:10.1111/j.2517-6161.1995.tb02031.x

155. M. E. Futschik, B. Carlisle, Noise-robust soft clustering of gene expression time-course data. *J. Bioinform. Comput. Biol.* **3**, 965–988 (2005). doi:10.1142/S0219720005001375 Medline

156. A. Kamburov, R. Cavill, T. M. Ebbels, R. Herwig, H. C. Keun, Integrated pathway-level analysis of transcriptomics and metabolomics data with IMPaLA. *Bioinformatics* **27**, 2917–2918 (2011). doi:10.1093/bioinformatics/btr499 Medline